Journal of Russian Laser Research, Volume 28, Number 2, 2007

CREATION OF A DIAGNOSTIC COMPLEX FOR THE CHARACTERIZATION OF CRYOGENIC LASER-FUSION TARGETS USING THE TOMOGRAPHY METHOD WITH PROBING IRRADIATION IN THE VISIBLE SPECTRUM

E. R. Koresheva,[1] I. E. Osipov,[1] I. V. Aleksandrova,[1] A. I. Nikitenko,[1] S. M. Tolokonnikov,[1] V. I. Listratov,[2] I. D. Timofeev,[2] A. I. Kupriyashin,[1] V. N. Leonov,[1] E. L. Koshelev,[1] G. D. Baranov,[2] G. S. Usachev,[2] T. P. Timasheva,[1] and A. I. Gromov[1]

[1] *P. N. Lebedev Physical Institute, Russian Academy of Sciences*
Leninskii Prospect 53, Moscow 119991, Russia
[2] *The Red Star State Enterprise*
Elektrolitnyi Proezd 1A, Moscow 115230, Russia
e-mail: koresh@sci.lebedev.ru

Abstract

We present our results on developing a diagnostic complex for high-precision characterization of the parameters of laser-fusion microobjects, such as microspheres and cryogenic targets (the microobject size is 1–2 mm). The complex operates based on the principle of tomography. The complex consists of (a) the scanning system providing a set of shadow projections of a microobject in the visible range of radiation and (b) specially developed software for 3D reconstruction of the microobject from the set of projections. The spatial resolution of the optical system is 1 μm for a probing-radiation wavelength of 490 nm. The distinctive features of the diagnostic complex are (1) operation with both free-standing and mounted targets and (2) the possibility of scanning the targets from room to cryogenic temperatures. The operation of the complex was demonstrated in the reconstruction of polystyrene microspheres by a large set (80–90) of shadow projections at room and cryogenic temperatures.

Keywords: tomograph, scanning system, imaging system, image projection data, bright band, reconstruction algorithm, inertial confinement fusion, cryogenic target, microshell.

1. Introduction

The prospects for development of inertial confinement fusion (ICF) are determined by reliable analysis of laser-experiment results. This, in turn, depends on the precise and unambiguous determination of the parameters of spatial microobjects, such as, for instance, a cryogenic target and laser-driven plasma. In this connection, the development of a reliable diagnostic system becomes top priority in ICF studies. In view of this, a program for developing diagnostic complexes based on tomographic methods of information processing was approved at the P. N. Lebedev Physical Institute [1,2]. The program was realized in years 2000–2004. The reasons for the program are as follows.

Translated from a manuscript submitted on May 17, 2006.
1573-8760/07/2802-0163

The cryogenic target is a system of nested layers, the simplest version of which is a polymer shell and a cryogenic layer of fuel. The diagnostics (characterization) of a cryogenic target is taken to be the determination of its parameters with high accuracy — deviation of the shell and layer from sphericity and concentricity, mass uniformity of the shell and layer, and local inhomogeneities on the surface of the shell and layer.

From the viewpoint of measuring the listed parameters, they are evidently local characteristics, i.e., they depend on the coordinates of the radius-vector **r** in the Cartesian coordinates, the origin of which coincides with the target center (Fig. 1). The means of control should provide the spatial reconstruction of the target with required accuracy. For instance, in the case of a cryogenic layer, the mass uniformity, sphericity, and concentricity should be better than 2%, and the local inhomogeneities on the surface of the condensed fuel should not exceed 1000 Å. If a cryogenic layer as a whole (i.e., for any values of **r**) satisfies the above conditions, then (in this and only this case) the layer can be said to have a certain thickness, density, and required surface quality. As the generally accepted diagnostic methods operate in one or several projections [3–7], they enable the assessment of only averaged (integral) values of the magnitudes. Transition to the local characteristics requires a new direction in the target diagnostic to be developed, one of which is based on the tomographic methods of information processing.

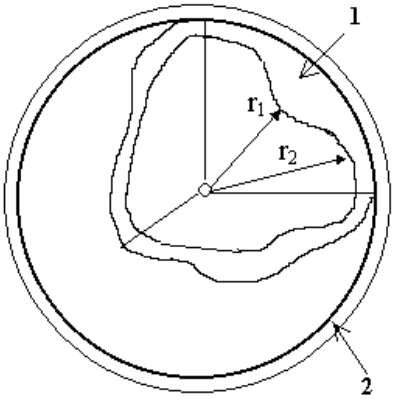

Fig. 1. Parameters of the cryogenic fuel layer with respect to the radius vector.

A schematic of the tomograph setup is shown in Fig. 2.

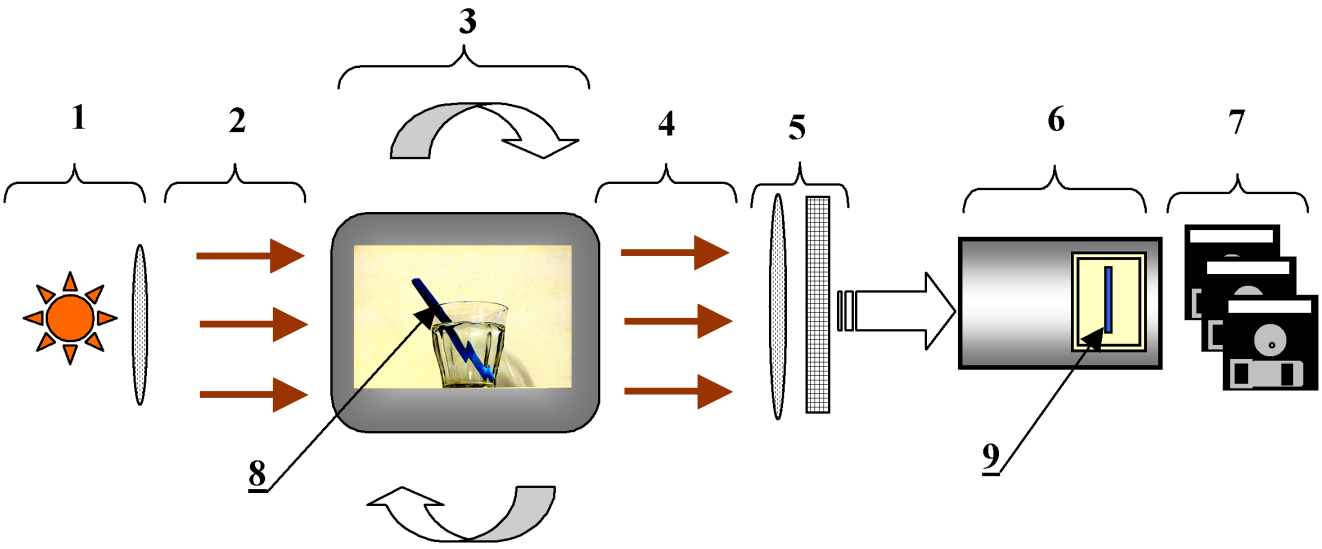

Fig. 2. A schematic of possible tomograph setup: probing radiation source (lighter) (1), incident radiation (2), scanning system (3), passed radiation (4), receiver (CCD camera) (5), computer with monitor (6), software programs to realize an object-reconstruction algorithm (7), object under study (8), and reconstructed image of the object (9).

The sequence of operations in the diagnostics of an object on the tomograph is as follows:

• A probing radiation or a signal is directed onto the object according to the chosen scanning protocol (the source of radiation is chosen depending on the nature of the object and can be laser radiation, X-rays or electron beams, optical radiation, etc.).

• Two magnitudes of the signal are measured — the first one before it interacts with the object and the second one after the signal passes through the examined object in each direction in the scanning plane (i.e., the characteristics or projections obtained are integral).

• The initial database, which represents a set of projections, is generated.

• The projections are processed by an algorithm enabling a set of local characteristics of the object to be produced, which is the final goal of solving the target's diagnostic problem.

Thus, the main parts of the tomograph are (i) the scanning system to obtain the required number of projections of a microobject and (ii) the algorithm for the spatial reconstruction of the structure (parameters) of the microobject based on the set of projections produced.

Our purpose in this study was to develop the software and component basis of the tomograph for unambiguous and highly precise diagnostics of the parameters of ICF microobjects, such as microspheres and cryogenic targets. Below we present our main results obtained while solving this problem.

2. Reconstruction Algorithm

2.1. Spectral Characteristics of the Microobject under Study

The algorithm for spatial reconstruction of a microobject is one of the main components in the tomograph setup. It is developed in parallel with the search for the optimum scanning protocol for a given probing source. The starting point, therefore, would be to choose the probing radiation source based on the analysis of the spectral characteristics of a microobject.

In fact, to choose a source means to find the mechanism of interaction between the radiation of a source and the material of a microobject. Herewith, a particular character of developing a diagnostic complex requires the evident and often mutually-excluding conditions to be satisfied:

1. The interaction between the radiation of a source and the microobject material should be sufficient to ensure its reliable recording.

2. The effect of the probing radiation on the measured parameters should be as small as possible during the diagnostics.

3. A real possibility of setting up the microobject image-recording system with required spatial resolution should be provided in the chosen range of wavelengths.

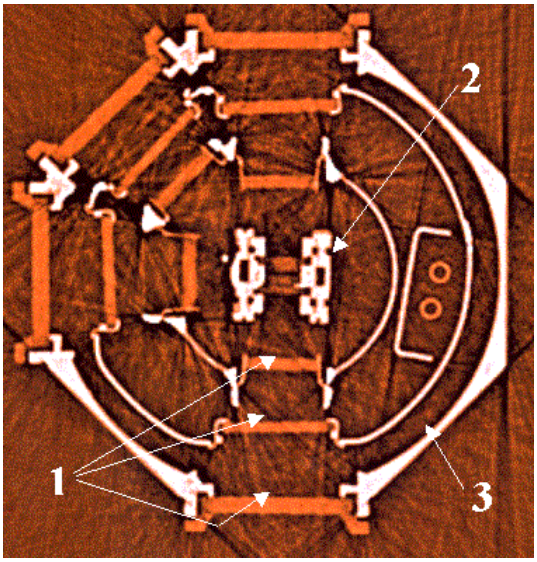

Fig. 3. Horizontal cross section of the cryostat at the site of the optical test chamber (obtained on a BT-50 tomograph): glass windows of the cryostat (with thickness of 2 mm) (1), test chamber (2), and outer wall of the cryostat (3).

We start with the X-ray region of the spectrum, since classical tomography (theoretically and experimentally, commercial tomograph including) has been developed exactly for this wavelength range; it is based on the absorption of X-rays in the specimen. This choice is not by chance; it is determined by the rectilinear propagation of probing X-radiation in the specimen medium. This presents certain advantages in the analysis of the physical principles and mathematical constructions, which are the basis of the inverse algorithm.

First of all, note that during the diagnostic process the cryogenic target should be inside the test chamber of the cryostat in the zone of helium temperatures. Since X-radiation possesses a significant penetrability, in the case of cryogenic targets, we should study the peculiar features of the spectral properties of not only the target material but also of the surrounded media, including liquid helium and the walls and windows of the cryostat.

As follows from Table 1, the ratio of absorption of X-radiation that passed through the shell of the target (polymer microsphere) and the cryogenic layer to that of X-radiation that passed through the walls (metal) and windows (glass) of the cryostat is too small to ensure a reliable recording of the object of interest. This is also confirmed by the results of observations conducted using a BT-50 commercial tomograph (Industrial Introscopy, Russia).

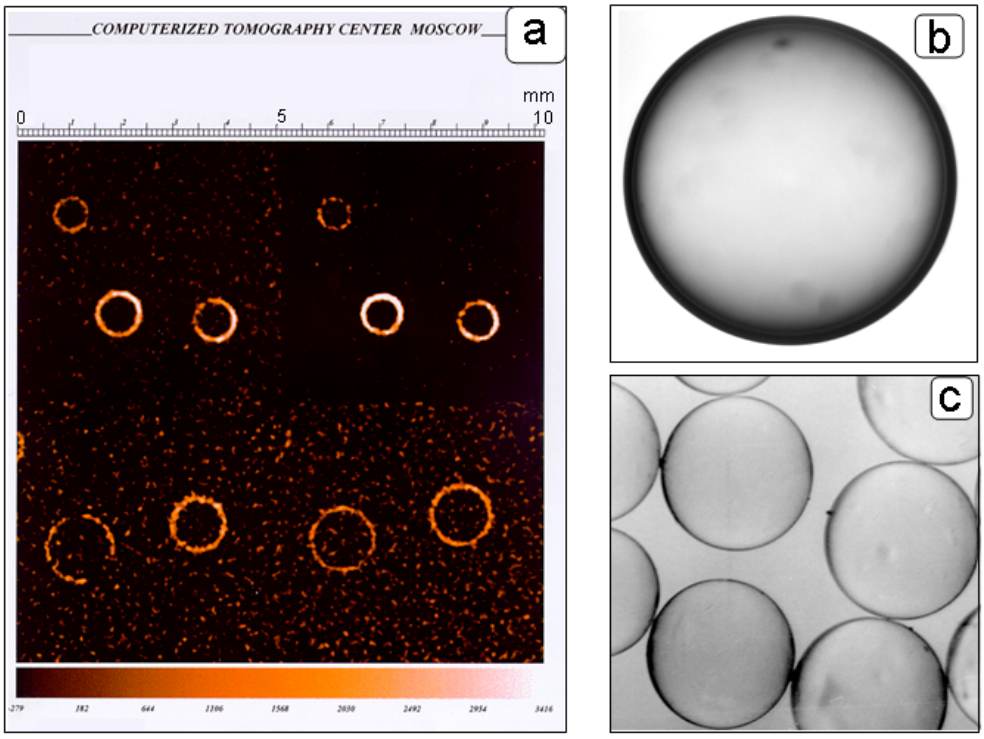

Fig. 4. Images of polystyrene microspheres in X-ray using BT-50 tomograph with voltage of 370 kV, current of 2 mA, and copper filter of 1.5 mm (a) and in the visible light using an IMTsL-100 microscope with a radiation wavelength of 0.4–7 μm (b and c).

Table 1. Mass Attenuation Factors μ/ρ in [cm^2/g], Attenuation Factors μ in [cm^{-1}], and Half-Value Thicknesses d in [mm] for Various Materials Depending on X-ray Wavelengths λ in [nm] [8, 14–16].

Parameter	Solid hydrogen $\rho = 0.089$ g/cm^3				Polystyrene $\rho = 1.05$ g/cm^3				Glass $\rho = 2.5$ g/cm^3			Copper $\rho = 8.96$ g/cm^3		
V, kV	1.0	3.0	6.0	10.0	1.0	2.0	3.0	12	1.0	2.0	12.0	1.0	10	20
λ	1.23	0.41	0.20	0.12	1.23	0.62	0.41	0.10	1.23	0.62	0.10	1.23	0.12	0.062
$\frac{\mu}{\rho}$	7.3	$5.6\cdot10^{-1}$	$4.0\cdot10^{-1}$	$3.8\cdot10^{-1}$	$2.8\cdot10^{3}$	$3.9\cdot10^{2}$	$1.2\cdot10^{2}$	5.9	$1.9\cdot10^{3}$	$2.3\cdot10^{3}$	4.8·10	$1.2\cdot10^{4}$	$2.2\cdot10^{2}$	3.3·10
μ	$6.5\cdot10^{-1}$	$5.0\cdot10^{-2}$	$3.6\cdot10^{-2}$	$3.4\cdot10^{-2}$	$3.0\cdot10^{3}$	$4.1\cdot10^{2}$	$1.2\cdot10^{2}$	6.3	$4.8\cdot10^{3}$	$5.8\cdot10^{3}$	$1.2\cdot10^{2}$	$1.1\cdot10^{5}$	$2.0\cdot10^{3}$	$3.0\cdot10^{2}$
d	$1.1\cdot10^{3}$	$1.4\cdot10^{5}$	$1.9\cdot10^{5}$	$2.0\cdot10^{5}$	2.3	1.7·10	5.7·10	$1.1\cdot10^{3}$	1.4	1.2	5.8·10	$6.1\cdot10^{-6}$	3.4	2.3·10

Figure 3 shows an Utrex-1-RTA cryostat in the horizontal cross section. The image of the polymer microsphere, really present in the center of the test chamber, is clearly missing. Using a BT-50 tomograph, we succeeded in producing only the images of the microspheres located outside the cryostat (see Fig. 4a). For comparison, Fig. 4b gives images of the polymer microspheres obtained using an IMTsL-100 microscope (the radiation wavelength is 0.4–7 μm).

Table 2. The Wavelength Corresponding to the Maximum of Absorption in the Cryogenic-Layer Material [17–19].

Isotope	H_2	HD	D_2	DT
λ, μm	2.11–2.43	2.57	3.16	3.46

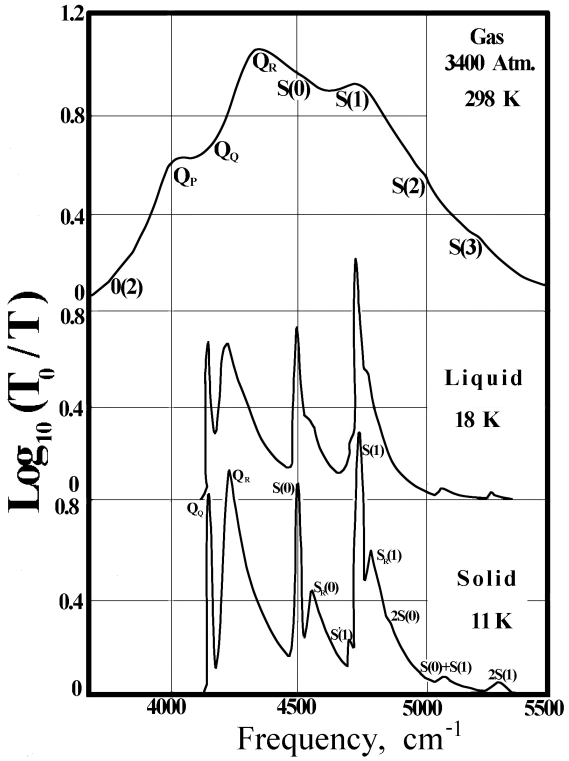

Fig. 5. IR absorption spectra for H_2 in gaseous ($T = 298$ K), liquid ($T = 18$ K), and solid ($T = 11$ K) states (data of [8]).

Another possibility of setting up a tomograph, based on the absorption, is to use the infrared (IR) range of the spectrum. In a certain spectral range, the absorption of IR radiation by the material of the cryogenic layer is significantly larger than for the X-ray range. Corresponding data are given in Table 2 and Fig. 5. On the other hand, the significant absorption of IR radiation makes noticeable the effect of probing radiation on the measured parameters of the target during the scan. Moreover, the cost of components of the target image-recording system for the given wavelength range is rather high.

Analysis suggested that the most reliable information on the quality of microobjects under study (at

a minimum impact of the radiation source on the object) could be obtained by using a probing radiation in the visible range of spectrum. In this case, the mechanism of interaction between the radiation and the object medium can be described predominantly based on the effects of light reflection and refraction.

2.2. Modeling of a Microobject and Development of a Direct Algorithm for Constructing the Microobject Image Using Its Parameters

When developing the reconstruction (inverse) algorithm, an important stage is the computer experiment to demonstrate its performance in the reconstruction of various test objects, such as, for instance, simulated images of single- and double-layer shells. To produce such test objects, we developed a 3D simulation model of the visible-radiation propagation through a multilayer shell. The model is based on the laws of geometrical optics, within the framework of which the path of each ray, involved in the formation of an image, is traced from the light source to the observation plane. Ray tracing, within the framework of this model, is based on the following relations:

- The shell under study is given by a set of 3D surfaces, which are three-axis ellipsoids:

$$\left(\frac{x^i - x_0^i}{a^i}\right)^2 + \left(\frac{y^i - y_0^i}{b^i}\right)^2 + \left(\frac{z^i - z_0^i}{c^i}\right)^2 = 1, \tag{1}$$

  where (x_0^i, y_0^i, z_0^i) is the center of an ith ellipsoid and (a^i, b^i, c^i) are its semiaxes. Here and below all distances are dimensionless and are referred to the maximum outer radius R of the shell, and all vectors are normalized to unity.

- A ray with directing vector $\mathbf{L} = (l, m, n)$ is emitted from point (x_0, y_0, z_0).

- The point of intersection (x_c, y_c, z_c) of the parametrically given ray with an ith surface is found by solving the system of equations

$$\begin{gathered}\left(\frac{x^i - x_0^i}{a^i}\right)^2 + \left(\frac{y^i - y_0^i}{b^i}\right)^2 + \left(\frac{z^i - z_0^i}{c^i}\right)^2 = 1, \\ x = x_0 + lt, \qquad y = y_0 + mt, \qquad z = z_0 + lt.\end{gathered} \tag{2}$$

  With respect to t, the system is reduced to the quadratic equation $At^2 + Bt + C = 0$, where

$$\begin{aligned} A &= b^{i2}c^{i2}l^2 + a^{i2}c^{i2}m^2 + a^{i2}b^{i2}n^2, \\ B &= 2\left(b^{i2}c^{i2}l(x_0 - x_0^i) + a^{i2}c^{i2}m(y_0 - y_0^i) + a^{i2}b^{i2}n(z_0 - z_0^i)\right), \\ C &= b^{i2}c^{i2}(x_0 - x_0^i)^2 + a^{i2}c^{i2}(y_0 - y_0^i)^2 + a^{i2}b^{i2}(z_0 - z_0^i)^2 - a^{i2}b^{i2}c^{i2}, \end{aligned} \tag{3}$$

  and further $x_c = x_0 + lt_c$, $y_c = y_0 + lt_c$, and $z_c = z_0 + lt_c$.

- In the intersection point (x_c, y_c, z_c), we plot $\mathbf{N}$ normal to the surface i

$$\frac{x_c - x_0^i}{a^{i2}} = \frac{y_c - y_0^i}{b^{i2}} = \frac{z_c - z_0^i}{c^{i2}}\,. \tag{4}$$

- The angle between the incident ray and the normal is determined as the arccosine of their scalar product $\phi = \arccos(\mathbf{L} \cdot \mathbf{N})$.

- The refracted and reflected rays (see Fig. 6) are calculated based on Snell's law $n_1 \sin\phi = n_2 \sin\psi$. Using Fig. 6, we find the normalized (unit) vector of the reflected ray

$$\mathbf{R_n} = \mathbf{L} - 2(\mathbf{L} \cdot \mathbf{N})\mathbf{N} \tag{5}$$

and the normalized vector of the refracted ray

$$\mathbf{D_n} = \frac{n_1}{n_2}(\mathbf{L} - \mathbf{N_s}) - \sqrt{1 - \left(\frac{n_1}{n_2}\right)^2 [1 - (\mathbf{L} \cdot \mathbf{N})^2]}\,\mathbf{N}. \tag{6}$$

- The intensity of refracted light is calculated by the Fresnel formulas

$$I_r = \frac{1}{2}\left(r_\parallel^2 + r_\perp^2\right) I_i, \quad \text{where} \quad r_\parallel^2 = \left[\frac{\tan(\phi - \psi)}{\tan(\phi + \psi)}\right]^2, \quad r_\perp^2 = \left[\frac{\sin(\phi - \psi)}{\sin(\phi + \psi)}\right]^2. \tag{7}$$

We can express the reflective indices $r_\parallel$ and $r_\perp$ through $\cos\phi$ as follows:

$$\begin{aligned} r_\parallel^2 &= \left[\frac{\cos\phi - N\sqrt{1 - N^2(1 - \cos^2\phi)}}{\cos\phi + N\sqrt{1 - N^2(1 - \cos^2\phi)}}\right]^2, \\ r_\perp^2 &= \left[\frac{\sqrt{1 - N^2(1 - \cos^2\phi)} - N\cos\phi}{\sqrt{1 - N^2(1 - \cos^2\phi)} + N\cos\phi}\right]^2. \end{aligned} \tag{8}$$

- The condition of total reflection reads

$$\sin\phi > n \quad \text{or} \quad \cos\phi < \sqrt{2 - \mathrm{n}^2}. \tag{9}$$

- The intensity of refracted light is

$$I_d = I_i - I_r. \tag{10}$$

- The change in intensity due to the light absorption in the medium reads

$$I_{\text{out}} = I_{\text{in}} \exp(-d/L_a), \tag{11}$$

where d is the dimensionless distance between two consecutive points of the ray intersection with the surfaces forming the shell, and $L_a = L/R$ is the dimensionless length of absorption for the corresponding layer.

- The incursion of the ray in an ith layer is

$$\psi = 2\pi dR/\lambda, \tag{12}$$

where λ is the light wavelength.

- The path of each ray inside the shell is traced until a given ray leaves the shell or its intensity becomes smaller than a preset threshold $I_i < I_{\text{lim}}$.

The final stage of tracing is to find the points of intersection with the observation plane for the rays that got into the preset aperture. When realizing the model as a computer program, the initial rays are generated with random coordinates in the source plane. This condition enables us to avoid numerous artifacts, which significantly distort the model shadow image.

Based on the model created, we developed two programs for constructing a shadow image from the known parameters of single- and double-layer spherical shells — 3D Ray Tracing and Shell Optics Model. The algorithms, in view of which the model is realized in these programs, are completely three-dimensional but have their own peculiar features. The capabilities and interfaces of the programs also differ. In combination, these programs satisfy the entire set of requirements necessary to solve the problem of forming an image of a transparent microobject by numerical modeling. Figure 7 shows the results of generating shadow and interference images of cryogenic targets using these programs.

The study of the correlation between the image of a real microsphere and its image generated, using the developed software, supported the adequacy of the model created (Fig. 8).

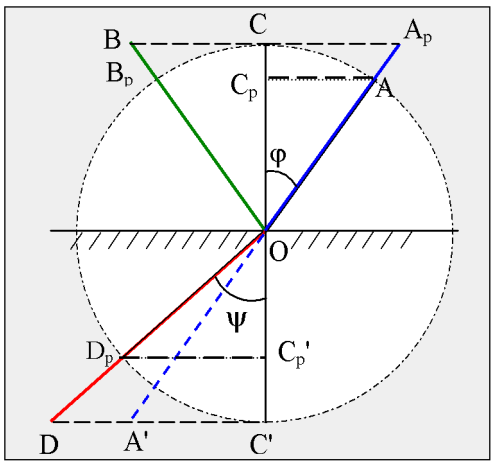

Fig. 6. Refracted and reflected rays calculated based on Snell's law. The following notation is used: AO = L is the incident unit ray, CO = N is the unit normal, $A_pO = L_1$ is the projection of the unit normal on the ray, $C_pO = N_s$ is the projection of the unit ray on the normal, BO = R is reflected ray, $B_pO = R_n$ is unit reflected ray, DO = D is refracted ray, $D_pO = D_n$ is unit refracted ray, φ is the angle of incidence, and ψ is the refraction angle.

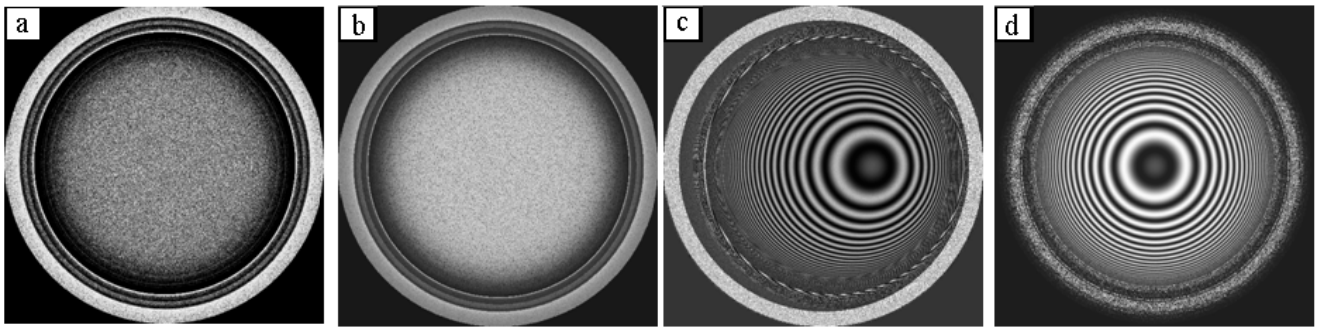

Fig. 7. Results of image modeling for cryogenic targets (double-layer shells) using the 3D Ray Tracing and Shell Optics Model software programs: Two-layer shell tomography with the ray-collection mode for the calculation parameters: $a_1 = 1$, $b_1 = 1$, $c_1 = 1$, $a_2 = 0.9$, $b_2 = 0.9$, $c_2 = 0.9$, $x_2 = 0$, $y_2 = 0$, $z_2 = 0$, $a_3 = 0.8$, $b_3 = 0.8$, $c_3 = 0.8$, $x_3 = 0$, $y_3 = 0$, $z_3 = 0$, $n_1 = 1$, $n_2 = 1.5$, $n_3 = 1.14$, $n_4 = 1$, $A = 60°$, and $I_{\text{lim}} = 0.01$ (a); Two-layer shell tomography with the ray-groups addition mode for the calculation parameters: $a_1 = 1$, $b_1 = 1$, $c_1 = 1$, $a_2 = 0.9$, $b_2 = 0.9$, $c_2 = 0.9$, $x_2 = 0$, $y_2 = 0$, $z_2 = 0$, $a_3 = 0.8$, $b_3 = 0.8$, $c_3 = 0.8$, $x_3 = 0$, $y_3 = 0$, $z_3 = 0$, $n_1 = 1$, $n_2 = 1.5$, $n_3 = 1.14$, $n_4 = 1$, $A = 60°$, and $I_{\text{lim}} = 0.01$ (b); Interference image of two-layer shell with the calculation parameters: $a_1 = 1$, $b_1 = 1$, $c_1 = 1$, $a_2 = 0.97$, $b_2 = 0.97$, $c_2 = 0.97$, $x_2 = 0$, $y_2 = 0$, $z_2 = 0$, $a_3 = 0.87$, $b_3 = 0.87$, $c_3 = 0.87$, $x_3 = -0.06$, $y_3 = 0$, $z_3 = 0$, $n_1 = 1$, $n_2 = 1.5$, $n_3 = 1.14$, $n_4 = 1$, $A = 60°$, $I_{\text{lim}} = 0.01$, $\lambda = 1600$ nm, and $R = 500$ μm (c); Interference image of two-layer shell with the calculation parameters: $a_1 = 1$, $b_1 = 1$, $c_1 = 1$, $a_2 = 0.97$, $b_2 = 0.97$, $c_2 = 0.97$, $x_2 = 0$, $y_2 = 0$, $z_2 = 0$, $a_3 = 0.87$, $b_3 = 0.87$, $c_3 = 0.87$, $x_3 = 0$, $y_3 = 0$, $z_3 = 0$, $n_1 = 1$, $n_2 = 1.5$, $n_3 = 1.14$, $n_4 = 1$, $A = 60°$, $I_{\text{lim}} = 0.01$, $\lambda = 1600$ nm, and $R = 500$ μm (d).

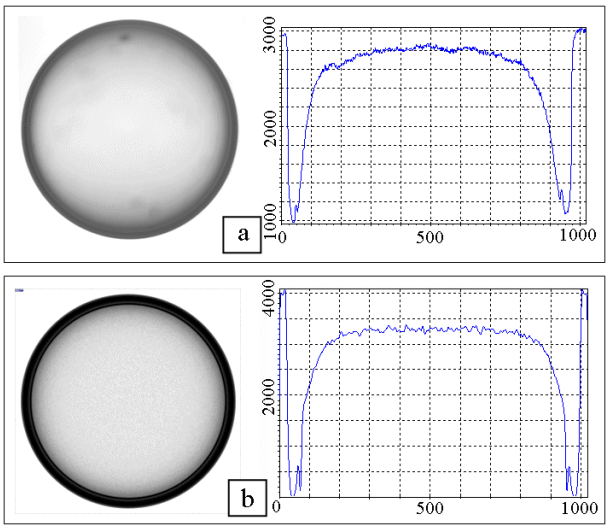

Fig. 8. Test of the direct algorithm: a real microsphere from polystyrene (a shadow projection on the left and a diameter-wise profile of intensity on the right) (a) and calculated image of the microsphere (left) and a diameter-wise profile of intensity (right) (b). Parameters of the microsphere: radius $R = 490$ μm, wall thickness $\Delta R = 14$ μm. Calculation by $120{\cdot}10^6$rays with the following parameters for surface 1: $a = 1.00$, $b = 1.00$, $c = 1.00$, $x_0 = 0.00$, $y_0 = 0.00$, $z_0 = 0.00$, and $n_1 = 1.60$ and for surface 2: $a = 0.93$, $b = 0.93$, $c = 0.93$, $x_0 = 0.00$, $y_0 = 0.00$, $z_0 = 0.00$, $n_2 = 1.00$, and $n_0 = 1.00$.

2.3. The Inverse Algorithm for 3D Reconstruction of the Parameters of a Microobject by the Bright-Band Position on Its Shadow Images (BBP Algorithm)

Using the created 3D light-propagation model, we studied the physics of shadow-image formation, in particular, the bright-band formation on images of transparent microspheres and cryogenic targets. The bright-band position and the intensity distribution were described by the methods of formal mathematics. Figure 9 (a and b) shows an analytic dependence, which enables the calculation of the thickness of the cryogenic layer or wall of a microsphere by the position of the bright-band-intensity maximum. Figure 9 (c and d) shows the position of the bright band on the shadow images of a cryogenic target and microsphere. Based on the results obtained, we developed an inverse algorithm for solving the problem of spatial reconstruction of microspheres and cryogenic targets by the bright-band position on the shadow projections (so-called BBP algorithm). A detailed description of the mathematical formalism in developing the BBP algorithm is given in [9, 10]. In accordance with the BBP algorithm, the reconstruction problem is split into several operations including:

1. Preprocessing to reveal the peculiar features of an image in each projection without distorting information;
2. Determination of the bright-band position and the shell edge for each projection;
3. Conversion of the coordinates for the band-brightness maximum to those of the inner surface;
4. Reconstruction of the inner surface and determination of the microobject parameters;
5. 3D visualization.

To perform these operations, we developed the software 'Target Studio' which includes the program 'Shell Explorer' for image preprocessing, the program 'Bright Ring' for finding the bright-band parameters and the program 'EasyView3D' for 3D visualization of the microobject reconstruction. Moreover, using

the Target Studio program, it is possible to determine such target parameters as the radius of the outer surface of the shell and its nonsphericity, the radius of the inner surface of the shell, thickness variation, as well as to obtain the profiles of arbitrary-diameter cross sections, the spectrum of spatial frequencies, etc. Figure 10 shows the main window of the Target Studio program and the window of the final result of the visualization program.

Let us consider the realization of the BBP algorithm using the created set of programs in more detail:

• It is assumed that the shape of the outer layer of the cryogenic target (i.e., microsphere) is spherically symmetric, and its outer radius and thickness are known. In the case of a single-layer shell, and its outer surface is a regular sphere. The refractive indices of each layer are also known.

• If required, the images are preprocessed using the Shell Explorer program (normalized, filtered, etc.).

• The initial data – the bright-band coordinates with respect to the shell edge depending on the angle – are obtained after the processing of the each-projection image using the Bright Ring program. The results obtained for each projection are recorded to a file of special format. Then these files are processed by the Target Studio program.

• Based on the parameters of a concrete target (the outer-layer thickness, refractive indices, etc.), the program calculates the dependence of the cryolayer thickness on the bright-band coordinate (see Fig. 9),

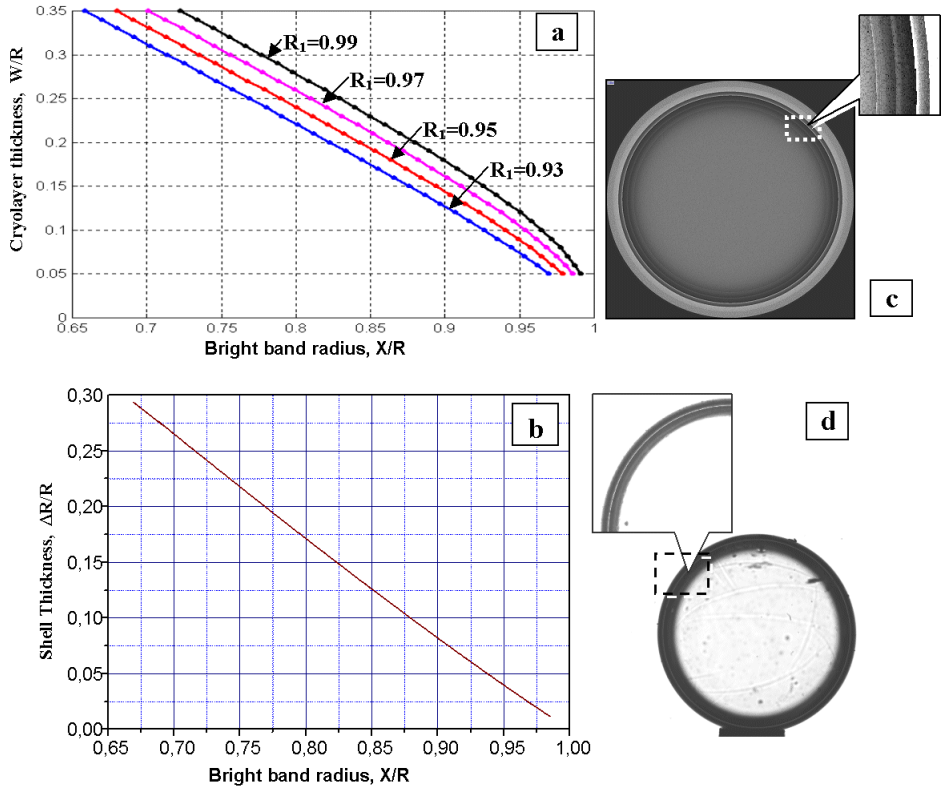

Fig. 9. Thickness of the cryolayer at various values of inner radius R_1 of the microsphere (a), wall thickness ΔR of the microsphere versus the position of the bright-band-intensity maximum (b), and bright bands on the images of the cryogenic target (c) and microsphere (d), respectively. Refractive index of the microsphere $n_1 = 1.5$, refractive index of the cryolayer $n_2 = 1.14$, and R is outer radius of the microsphere.

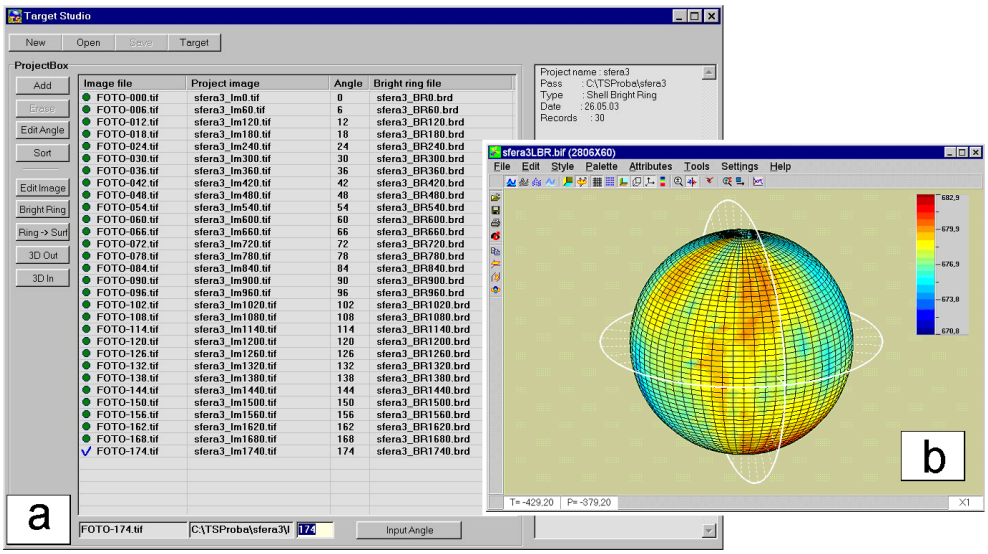

Fig. 10. Main window of the Target Studio program (a) and the window of the final-result visualization program (Easy View 3D) (b).

which will be further used to determine the local thickness of the cryolayer. This is done once for all projections.

• The next stage is to read the earlier recorded files and to reduce (interpolate) the data they contain to a uniform grid in the coordinates of the ascent and azimuthal angles; the grid step is different for each coordinate. This stage is required since the number of points for each projection can be different, and their step can be variable, because some points can drop out due to the image defects.

• A local thickness of the cryogenic layer is assigned to each number from the rectangular matrix obtained (this number is nothing else that the local coordinate of the bright band), using the preliminarily calculated dependence of the cryolayer thickness on the bright-band position. As a result, another rectangular matrix is constructed, each number in which is a local position of the inner surface of the cryolayer. These data are recorded to a separate file.

• The final result can be visualized using the EasyView3D program. It is written based on the Open Global Library and enables presenting the functions of two variables as 3D surfaces both in Cartesian and spherical coordinates. A possibility of magnifying and arbitrarily rotating the object, a profound level of its details, change of shape and presentation attributes, etc. are provided.

The BBP algorithm and Target Studio programs were tested as follows.

Using the Shell Optics Model program, a set of 60 cryotarget projections evenly arranged at steps of 6° was generated. A double-layer shell (cryogenic target) with the following parameters was used as a test shell. The outer layer (glass microsphere) was spherically symmetric, its inner radius $R_{\rm i} = 0.94$ (here and further all linear sizes are given in units of the target's outer radius $R_{\rm out} = 1$), and the refractive index $n = 1.5$. The inner surface of the cryogenic layer is a three-axis ellipsoid with semiaxes in X, Y, and Z equal to $a = 0.8$, $b = 0.76$, and $c = 0.82$, respectively, shifted off-center by $\Delta x = 0.01$, $\Delta y = 0.05$, and $\Delta z = -0.02$. The refractive index of the second layer was 1.14 (solid DT mixture). The observation aperture was 25°. Gaussian diffusion by 5×5 matrix was used in modeling. The simulated image of the

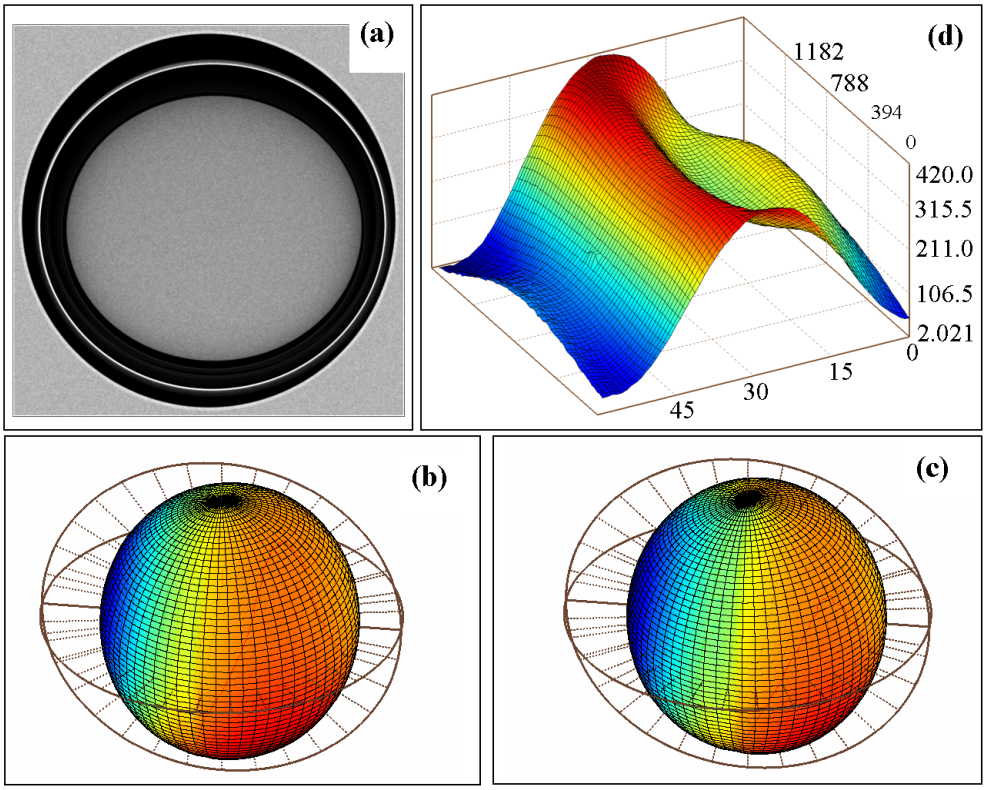

Fig. 11. Results of testing the BBP algorithm: image of the projection of the double-layer shell with scanning angle 78° (a), initial surface of the microsphere (b), microsphere surface reconstructed by a set of simulated projections (c), and the difference between the reconstruction result and the initial surface (d). The numbers in the Z axis are the percentages of the difference multiplied by 100 and shifted to the positive domain.

shell in one of the projections is shown in Fig. 11a. The testing results showed the mean deviation of the reconstructed surface from the initial surface to be about ±1% of the target's radius (Fig. 11b, c, and d).

3. Analysis of the Features of Forming Real Shadow Images of Microspheres and Cryogenic Targets. Technical Expertise for Creating a Diagnostic Complex

The purpose of our studies presented in this section was to formulate the technical requirements on the components of a diagnostic complex based on the tomography principle (or, simply, a tomograph). The complex should be capable of determining the parameters of a cryogenic target with a spatial resolution of 1–2 μm.

The main components of a tomograph are:

- a probing radiation source (or a lighter);
- the microobject scanning system;
- the image-forming system (or the optical system).

3.1. Main Limitations on the Technical Solution of the Diagnostic-Complex Components

To characterize a cryogenic target, it is necessary to determine the parameters of the following two microobjects: (1) a microsphere (the shell of a target) and (2) a spherical fuel layer inside the microsphere. As a rule, the microsphere parameters are determined at room temperature (300 K), whereas the fuel layer can be characterized only when the microobject is at cryogenic temperatures ($T < 20$ K).

The arrangement of the cryogenic target inside the test chamber of the cryostat is schematically shown in Fig. 12. The specific features of the operation with a cryogenic microobject require the following (often mutually excluding) conditions to be satisfied.

First, when characterizing the cryogenic layer the cryogenic target is constantly present in the zone of helium temperatures inside the optical test chamber of the cryostat, while the objective lens of the observation system is located outside the cryostat (see Fig. 12). Hence there is a limitation on the minimum admissible focal distance F of the objective lens, which forms the target's image.

Moreover, the high-quality image of a target is limited by the optical windows in the cryostat's test chamber (i.e., additional reflecting and refracting surfaces in the image-forming system), which rules out the possibility of rotating the cryostat together with the target with respect to the light beam without corresponding compensators for each scanning angle. Therefore, the only possibility to make scanning feasible in operations with a cryogenic target is to rotate the target with respect to probing radiation at a stationary cryostat.

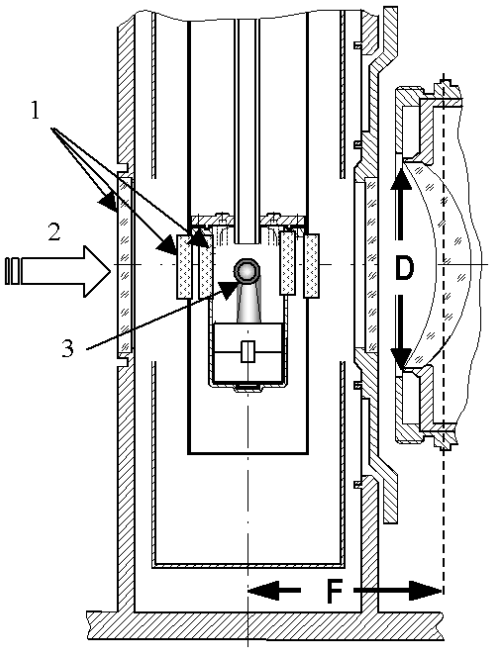

Fig. 12. Schematic of the arrangement of a cryogenic target inside the optical test chamber of a cryostat with D, diameter of the window (linear aperture of observation) and F, minimum admissible focal distance: windows (1), light (2), and target (3).

Further, for the maximum spatial resolution (D/F) to be realized, the diameter D of the objective lens should be sufficiently large at a corresponding large diameter of the cryostat windows and a small focal distance F. In contrast, to preserve the required level of temperature inside the test chamber and to keep the cryogenic-target parameters, the cryostat windows should be sufficiently small to satisfy the conditions of minimum infiltration heat from room radiation.

Thus, the essential problems in setting up a tomograph for cryogenic targets are (a) the development of a new design of the cryostat's test chamber to satisfy the requirements of high spatial resolution and preserve the layer parameters and (b) the development of a small-size target-positioning device to be operated at cryogenic temperatures and, if required, under high vacuum.

The listed problems show that the technical solution of the problem of characterizing the fuel layer inside the cryogenic target is much more complicated than the solution of the problem of characterizing the microsphere at room temperature. Therefore, a diagnostic complex consisting of two different tomographs was created for characterizing two different components that comprise the cryogenic target (the microsphere and cryogenic layer).

3.2. Requirements to the Probing Radiation Source

The important part of the tomograph is the probing radiation source (or the lighter). Above (see Sec. 2.1) we explained the choice of the probing radiation wavelength (the visible spectrum). In this section, we consider the main requirements to the source, which are dictated by the peculiar features of the reconstruction algorithm (BBP algorithm) we developed.

3.2.1. Coherence, Divergence, and Homogeneity of Radiation

First of all, consider the issue of required coherence of radiation. It is well known that the use of a coherent radiation source (laser) leads to the following:

- Numerous diffraction rings and fringes are observed on the shadow image of an object; they occur close to the zones of a sharp change in the wave-front intensity.
- The position, intensity, and configuration of these rings and fringes, as a rule, change significantly even at a slight variation – apertures, observation planes, etc.
- In a real experiment, speckles and parasitic interference fringes are present on the image, which is due to the light reflection from the structure components.

Thus, the use of coherent lighting to produce shadow projections of a microobject complicates both the experiment and the interpretation of images. At the same time, within the framework of the developed BBP algorithm, we cannot use the main advantage of coherent optics – information on the light-wave phase; hence the need to fulfill the requirement that probing radiation should be incoherent. From the viewpoint of producing the maximum spatial resolution of the optical system using visible radiation, a reasonable choice of the wavelength is the blue–green region of the spectrum (440–520 nm).

The geometry and intensity of the lighting beam are determined by the requirements to decrease the energy input to the test cryogenic chamber (with the view to keeping the cryotarget intact). On the strength of this, the light-spot diameter should be close to that of the microobject studied.

Since the BBP algorithm assumes that the conditions underlying the developed mathematical model of light propagation through a microobject are satisfied, the probing radiation should be close to a collimated beam. The admissible angle of divergence of the light beam is $2\omega < 0.028 = 96$ arcmin, which is determined from the condition of equality of the geometrical divergence of the beam to the value of the corresponding diffraction scattering of the bright band.

Using the numerical model of light propagation through a microobject, we investigated the effect of radiation inhomogeneity on the bright-band position in the image of a cryogenic target. The main conclusion was that an increase in the radiation inhomogeneity has no effect on the bright-band position, which carries information on the cryolayer surface.

3.2.2. Effect of Radiation Dispersion

The procedure for finding the refractive indices was as follows.

The known refractive indices of hydrogen [8] and polysterene [14] were used to find the values of A and B in the simplified Cauchy formula $n \cong A + B/\lambda^2$. Then, using this formula with corresponding values of A and B, we assessed the values of refractive indices for hydrogen and polystyrene at wavelengths of 0.44 and 0.65 μm (Table 3). The obtained values of the refractive indices were used to generate two shadow

images of the cryogenic target with the following parameters: $a_1 = b_1 = c_1 = 1$, $a_2 = b_2 = c_2 = 0.94$, $a_3 = b_3 = c_3 = 0.84$, $n_0 = n_3 = 1$, aperture 30°, and 150 million rays. The distinctions of the images from each other are shown in Fig. 13. Remarkably, the effect of dispersion on the groups of rays responsible for the formation of bright bands and the central part of the image is different. The diameter of the bright bands is larger in the image obtained in blue light ($\lambda = 0.44$ μm, line 1 in Fig. 13), whereas the diameter of the central part is larger in the image obtained in red light ($\lambda = 0.65$ μm, line 2 in Fig. 13). When illuminating an object with white light, the dispersion leads to some blurring of its image. To avoid this, in photographing an object, one should use radiation close to monochromatic or to use a light filter, which narrows the wavelength range of the lighter.

Table 3. Calculated Values of the Refractive Index n Versus the Radiation Wavelength λ.

Material	A	B	$\lambda = 0.44$ μm	$\lambda = 0.65$ μm
Solid hydrogen	1.132774	0.001051	$n = 1.1382$	$n = 1.1353$
Polystyrene	1.546580	0.015079	$n = 1.6245$	$n = 1.5823$

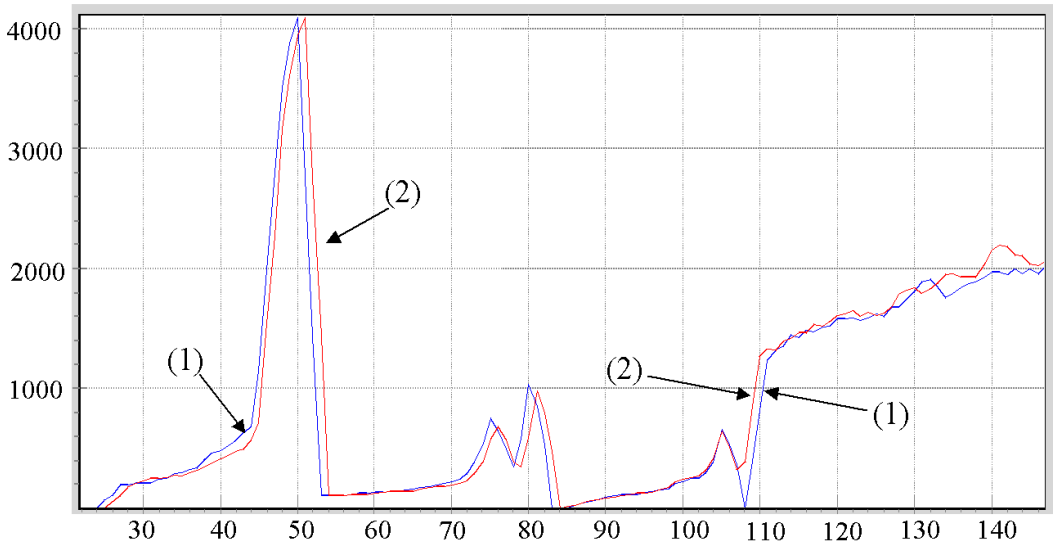

Fig. 13. A fragment of the diameter-wise image recording of a cryogenic target for $\lambda = 0.44$ μm (1) and $\lambda = 0.65$ μm (2).

3.2.3. Effect of Polarization

Achieving the maximum spherical symmetry of the constituent layers in the target is the main problem of the target technology. The aim of the characterization is to find and measure with maximum possible accuracy even very minor deviations from spherical symmetry in the shape of the target layers.

A beam of polarized light is nonsymmetric with respect to its axis. Therefore, the distribution of the polarization state in the image plane for polarized light would be nonsymmetric even in the case of an ideal shell. Since polarized light violates the natural symmetry of the problem, its use would only hinder

finding and measuring the target's deviations from symmetry. Therefore, the probing radiation of the tomograph for the targets should be unpolarized. Only in this case would a shadowgraph of an ideal target be symmetric with respect to the center, and any deviation from this symmetry would serve as a measure of its nonideality and a subject of measuring.

3.3. The Image-Forming System

3.3.1. Choice of the Observation Aperture

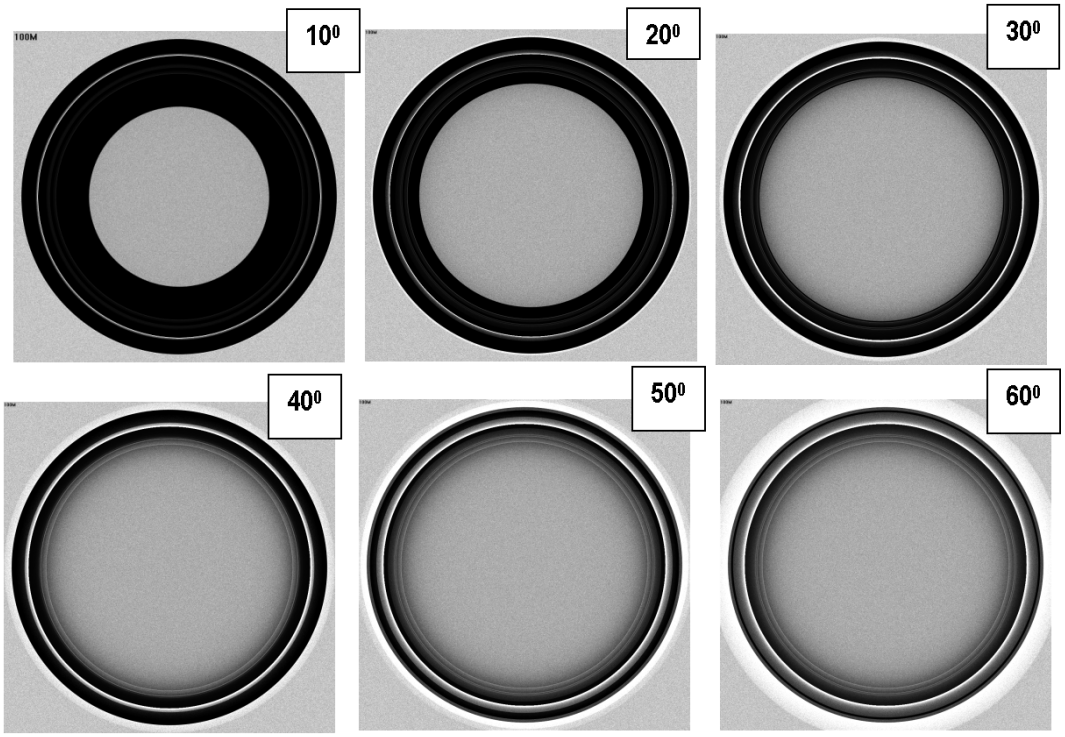

Fig. 14. Synthesized images of a cryogenic target for various observation apertures (shown at the top right of each image), where R_1 and R_2 are the inner radii of the microsphere and the cryogenic layer, respectively (given in units of the microsphere's outer radius). Parameters of the target: $R_1 = 0.95$, $R_2 = 0.8$, $n_0 = 1$, $n_1 = 1.5$, $n_2 = 1.14$, and $n_3 = 1$.

Using the computer program 3D Ray Tracing, we synthesized images of a double-layer shell (a cryogenic target) for various observation apertures. Figure 14 shows synthesized images of a cryogenic target with the following parameters: $R_1 = 0.95$ (the radius of the inner surface of the microsphere in units of the target's outer radius), $R_2 = 0.8$ (the radius of the inner surface of the cryolayer in units of the target's outer radius), $n_0 = 1$, $n_1 = 1.5$, $n_2 = 1.14$, and $n_3 = 1$ (here n_0, n_1, n_2, and n_3 are the refractive indices of the medium outside the target, the material of the microsphere, cryogenic layer, and the target's inner cavity, respectively). Each image was produced using 10^8 input rays.

Comparative analysis shows that a reduction of the observation aperture makes it possible to determine the bright-band position with a greater accuracy and, therefore, to reconstruct more exactly the position of the inner surface of the cryolayer using the BBP algorithm. On the other hand, the increase

in the aperture enables enhancing the spatial resolution of optical observation. Thus, when setting up a tomograph, it is desirable to take into consideration the possible changes in the observation apertures within sufficiently broad limits (from 10° up to 60°).

3.3.2. Requirements on the Photoreceiver Matrix

At present, mainly matrix photoreceivers are used for receiving images. Geometrically they are characterized by the matrix size $N\times M$ in pixels and the pixel size $\Delta x\times\Delta y$ (very often $\Delta x = \Delta y$). The dynamic range of the image produced is determined by the digit capacity of the analog-to-digital converter. In this work, we used B&W photoreceiver matrices of 1000×1000 pixels in size, with square pixels and 12-bit dynamic range (4096 levels of gray).

The 2D light field with the intensity distribution $I(x, y)$, incident on the photoreceiver, is converted into a matrix of numbers. In this conversion, distortions occur and the produced matrix $W[i, j]$ is not completely similar to the initial distribution of intensity $I(x, y)$, i.e.,

$$W[i, j] \neq I(i\Delta x, j\Delta y), \qquad i = 0, \ldots N, \quad j = 0, \ldots M. \tag{13}$$

This is mainly due to three phenomena — pixelation, noises, and final dynamic range.

The numerical values of the matrix $W[i, j]$ are produced by 2D integration of $I(x, y)$ by the area of an individual light-sensitive element of the photoreceiver matrix. The discrete image $W[i, j]$ can be considered as the result of 2D convolution of the initial image $I(x, y)$ with the pulse response of a separate pixel $P(x, y)$ (in our case, a symmetric rectangular function) followed by the sampling of this convolution in the final region (the matrix area) using the delta function

$$W[i, j] = [I(x, y) \otimes P(x, y)]\delta(x - i\Delta x,\, y - j\Delta y). \tag{14}$$

The initial distribution of intensity $I(x, y)$ can be reconstructed from (14) by spatial interpolation or by using the linear spatial filtration of the discrete image.

Let $\omega_p = 2\pi K/\Delta x$ be the image sampling frequency and ω_I be the maximum spatial frequency of the initial intensity distribution. It is evident that for round objects (the image of a cryotarget) $K \leq \min N, M$. According to the Nyquist criterion, if $\omega_I \leq \omega_p/2$, the initial image can be exactly reconstructed; otherwise, it is impossible. This means that the sampling step should not exceed half of the period of the spatial harmonic corresponding to the very fine details of the image.

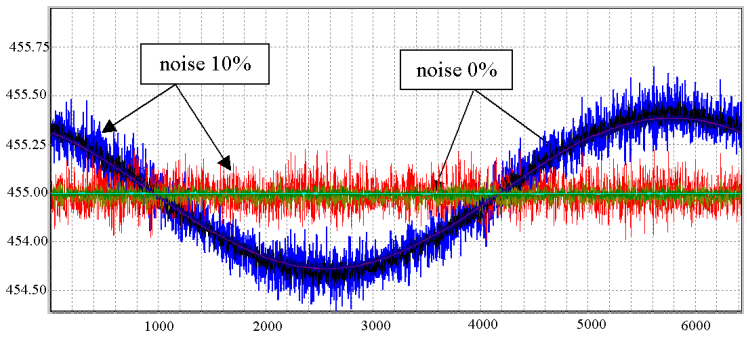

Fig. 15. Determination of the bright-band position by the test image. Curves are the first determination and straight lines are those after recalculating the center position. The numbers below are the noise amplitudes.

If the diameter of a cryogenic target is 1000 μm, and 1000 pixels fall into the diameter of its image, then we can reliably reconstruct details with the linear size ≥ 2 μm. Note that this number cannot be considered as the maximum accuracy of determining the position of some characteristic peculiarities of the cryotarget image – the edge, bright band etc.; it characterizes only the possibility of revealing small local defects.

Studies conducted using the direct algorithm showed that the discrete character of a correctly processed image is not an obstacle for a rather exact reconstruction of parameters of interest by the BBP algorithm. The size of one sensitive element (pixel) of the matrix can be several micrometers; herewith, the accuracy of reconstruction can reach fractions of a micrometer in the absence of noises (see Fig. 15).

An essential factor that worsens the reconstruction accuracy of a real image from its digital image is noise. The main source of noise is thermal generation of electrons in the photoreceiver-matrix cells. This noise is additive Gaussian noise by its nature. The amplitude of the noise component on real images can reach 1–5%; in this case, the noise significantly exceeds the sampling interval.

Based on the analysis conducted, we can formulate the following requirements on the CCD photoreceiver matrix:

- the matrix size is $\geq 1000\times1000$ pixels;
- the sensitive-element size is to be several micrometers;
- forced cooling of matrix to reduce noise is desirable.

From the viewpoint of minimizing the image-reconstruction error, it is required that the spatial and temporal inhomogeneities of the probing radiation not exceed the noise level of the photoreceiver CCD matrix.

3.3.3. Orientation of the Probing Radiation with Respect to the Photoreceiver Matrix

Let us assess now to which accuracy the direction of probing-radiation propagation should coincide with the orientation of the photoreceiver CCD matrix.

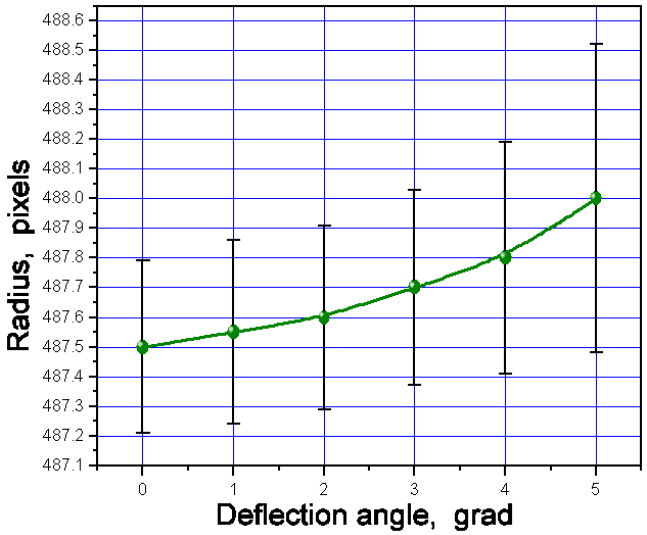

Fig. 16. Dependence of the average radius on the angle between the axes of the lighter and photosensor.

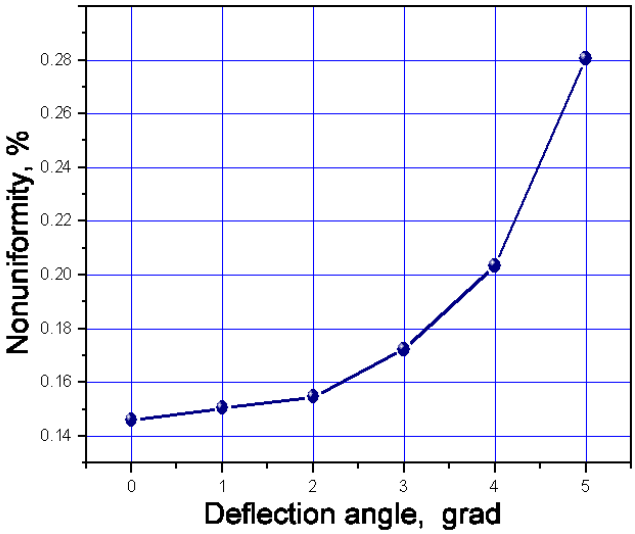

Fig. 17. Dependence of the radius inhomogeneity on the angle between the axes of the lighter and photosensor.

To determine the effect of the angle between the lighter axis and the normal to the photoreceiver plane on the accuracy of measuring the target parameters using the 3D Ray Tracing program, we generated six images (by 50 M rays each) of an ideal double-layer target ($a_1 = b_1 = c_1 = 1$, $a_2 = b = c_2 = 0.94$, $a_3 = b = c_3 = 0.84$, $n_0 = n_3 = 1$, $n_1 = 1.5$, $n_2 = 1.14$, and aperture 30°) at small values of α (0°–5°). After that, using the Shell Explorer program, we calculated the values of the mean radius and

its homogeneity $100(R_{\max} - R_{\min})/(R_{\max} + R_{\min})$ in percent for these images. It is seen in Fig. 16 that the mean radius depends weakly on the value of angle α, and its change lies within the limits of the measurement error. This was to be expected, since the radius is calculated by averaging a large number of values. The dependence of the inhomogeneity of the radius between the axes of the lighter and photoreceiver is much more pronounced (see Fig. 17).

Figure 18 illustrates the change in symmetry of the ideal target image at the occurrence of an angle between the lighter axis and the normal to the receiver-matrix plane. Using the Bright Ring program, we determined the position of the bright-band maximum for angles 0°, 1°, and 2°. In Fig. 19, the hatched zone corresponds to an accuracy of 1 μm at a ratio of 1 pixel $\approx$ 1 μm (the shell 1 mm in diameter, the photoreceiver CCD matrix 1000×1000 pixels). It is clear from this figure that the angle between the axes of the lighter and photoreceiver should not exceed ∼0.8°.

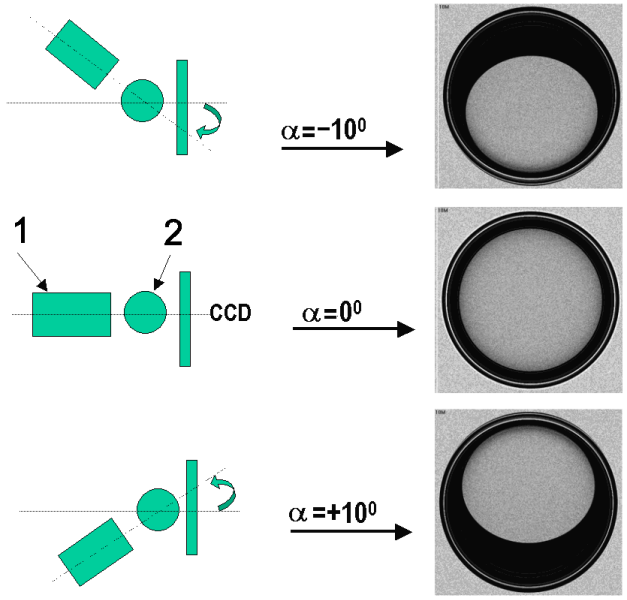

Fig. 18. Asymmetry of the image of an ideal target at off-axis illumination: lighter (1) and target (2). The images of the target were reconstructed using 10^6 rays.

3.4. Concluding Remarks on Technical Requirements on Tomograph

Analysis of the peculiarities of forming a shadow image of ICF microobjects (microspheres and cryogenic targets) enables us to formulate the technical requirements on the diagnostic system based on the tomography principle:

1. The system of optical observation should provide a spatial resolution of 1–2 μm in one projection.
2. The probing radiation is incoherent unpolarized radiation of the visible spectrum (wavelength ∼440–520 nm) with a collimated beam with spatial divergence of ≤96 arcmin.

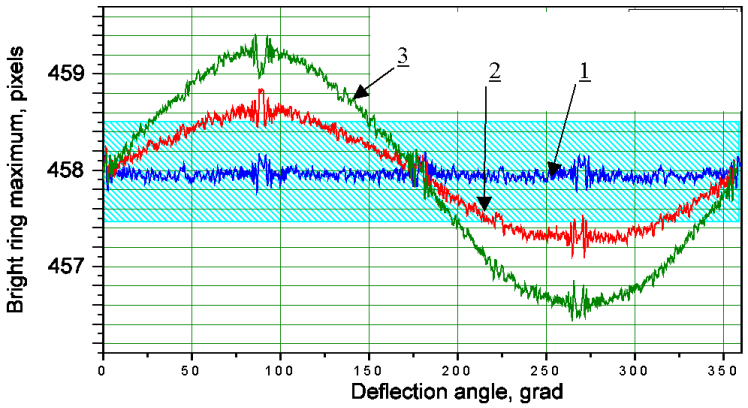

Fig. 19. Dependence of the bright-band position on the polar angle for various angles between the axes of the lighter and photosensor: 0° (1), 1° (2), and 2° (3).

3. The diameter of the light spot is close to that of the microobject studied.

4. The observation system should provide the possibility of changing the optical observation aperture within the range from 10° up to 60°.

5. The main requirements on the photoreceiver CCD matrix are:

   - the matrix size is $\geq$1000×1000 pixels;
   - the sensitive-element size is of several micrometers;
   - forced cooling of the matrix to reduce noise is desirable.

6. Misalignment of the axes of the probing radiation and the normal to the plane of the photoreceiver matrix should not exceed 0.8°.

7. Spatial and temporal inhomogeneities of the probing radiation should not exceed the level of noise of the photoreceiver matrix.

8. While characterizing the cryogenic layer, the scanning system should provide target rotation inside the stationary cryostat; the positions of the source and photoreceiver should be fixed.

9. The essential components of a tomograph for cryogenic targets are:

   - the tomographic test chamber (TTC), the construction of which simultaneously conforms to the requirement of high spatial resolution and the requirement of preserving the quality of the cryogenic layer in the measuring process;
   - the micromanipulator mounted inside the TTC, which makes it possible to produce a set of shadow projections and provides target rotation inside the stationary cryostat.

4. Diagnostic Complex for Tomography of Microspheres and Cryogenic Targets

In accordance with the technical specifications formulated above, a diagnostic complex for the tomography of ICF microobjects was created at the P. N. Lebedev Physical Institute jointly with the Red Star Federal State Unitary Enterprise. The complex includes the Shell Tester and FST Tester tomographs complete with specially developed software (Target Studio). The Shell Tester tomograph is intended for characterizing microspheres pneumatically fixed on a capillary. The microsphere during the tomography process is at room temperature (300 K). The schematic diagram and general view of the setup are shown in Fig. 20a. The FST Tester tomograph is intended for diagnostics of free-standing microspheres and cryogenic targets. The scanning system operates with the microobjects at room (300 K) or cryogenic (77–4.2 K) temperatures. The general view of the setup is shown in Fig. 20b. A brief description and technical specifications of the main components of the diagnostic complex are given in Appendix.

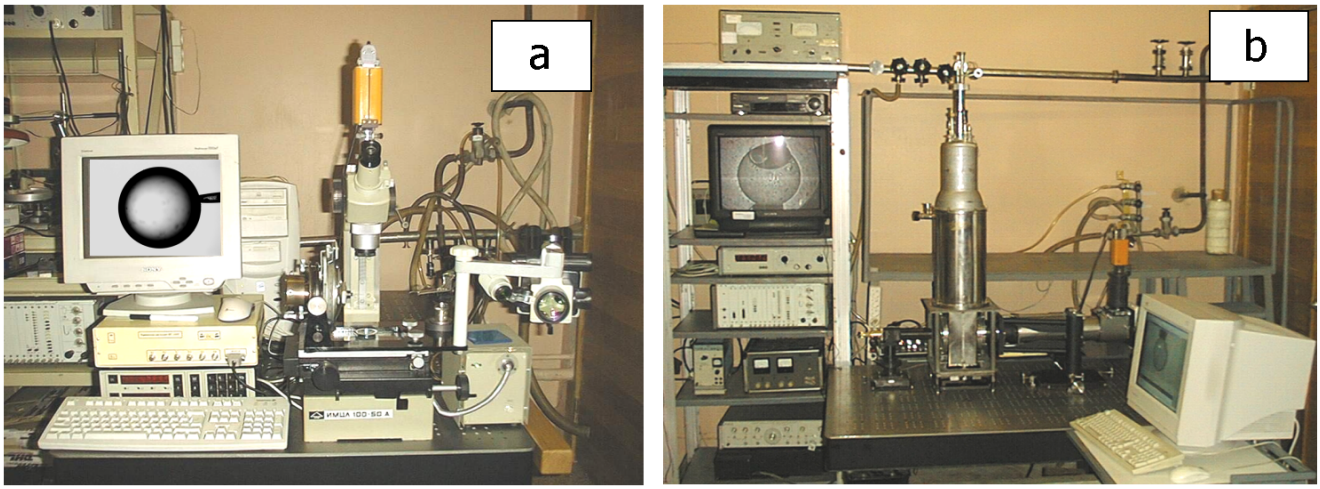

Fig. 20. A diagnostic complex for precise characterization of the parameters of laser-driven fusion microobjects by tomography methods: Shell Tester tomograph for work with mounted microspheres at 300 K (a) and FST Tester tomograph for work with unmounted (free-standing) microspheres and cryogenic target (b) at room (300 K) or cryogenic (4.2–77 K) scanning temperature of a microobject.

Tests have shown that the created complex possesses unique operational parameters including:

Temperature of microobject	room or cryogenic (77–4.2 K);
Wavelength of probing radiation	475±15 nm and 490±7 nm;
Complete microobject-scanning angle	360°;
Microobject positioning precision	±(1.5–2.5) arcmin;
Current number of projections, maximum	100;
Spatial resolution of the optical system in first projection	1–1.5 μm;
Diameter of microobject studied	1–1.5 mm.

A distinctive feature of the setup is the possibility of optimizing the conditions for forming a shadow image of a microobject by changing the following parameters within a broad range — the optical system aperture, angular divergence of the radiation source, intensity of scanning radiation, position of the object plane with respect to the microobject, etc.

Below we present the results of optimizing the conditions of forming the projection database for the subsequent reconstruction of the parameters of a microobject (microsphere) by the BBP algorithm using the specially developed software Target Studio.

4.1. Position of the Observation Plane: a Method of Adjustment to the Equatorial Plane of the Shell to Reduce the Systematic Error for a Set of Projections

In scanning, it is impossible to avoid displacement of the shell with respect to the optical-system components due to the imperfect fabrication of manipulating devices, as well as shift of the optical components due to different factors (temperature variations, vibrations). Shift in the direction perpendicular to the optical axis makes the shell move beyond the field of vision. These displacements can be easily

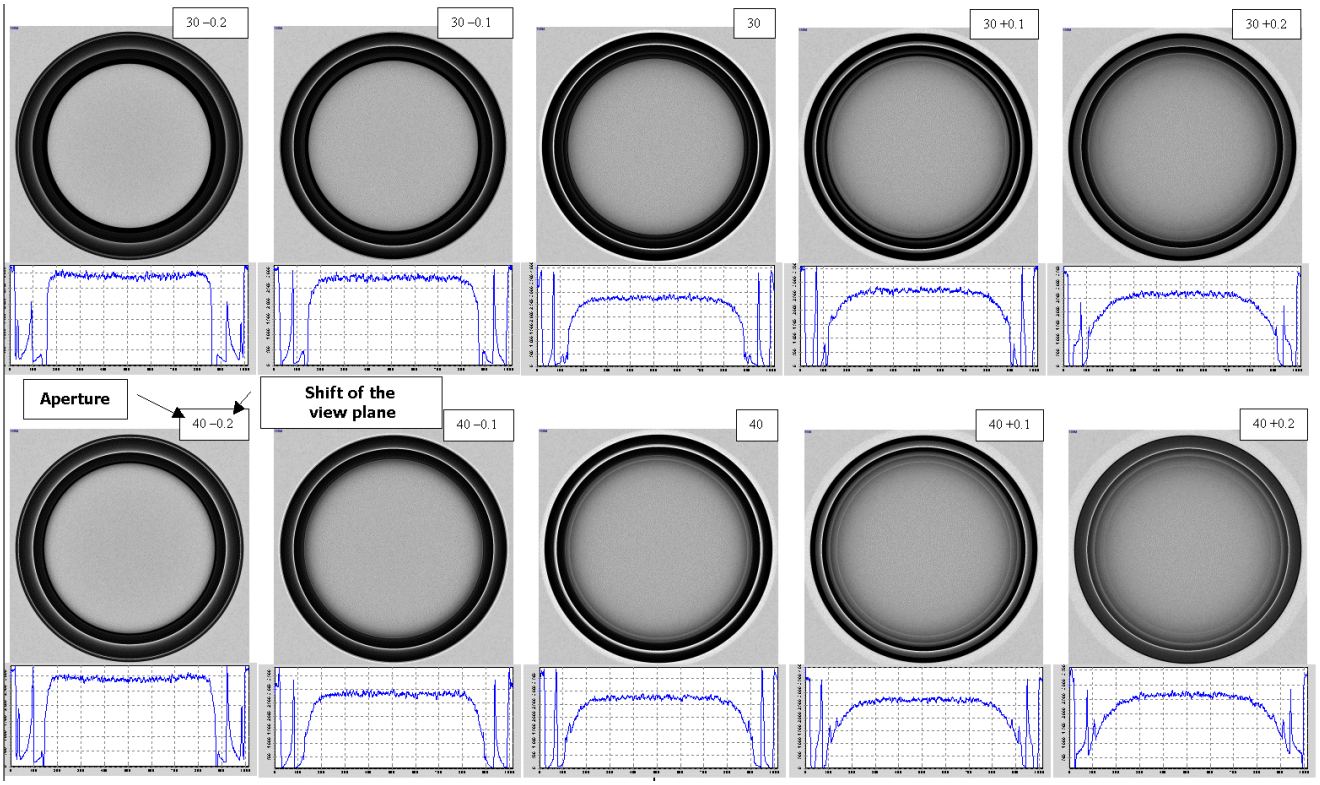

Fig. 21. Effect of the observation-plane position on the quality of the shadow image of a double-layer shell (cryogenic target). Images of a double-layer shell (a microsphere and a spherical cryolayer) with parameters $R_1 = 0.95$ (outer radius of the microsphere), $R_2 = 0.8$ (inner radius of the microsphere), $n_0 = 1$, $n_1 = 1.5$, $n_2 = 1.14$, and $n_3 = 1$ for various apertures and observation-plane positions were obtained using the 3D Ray Tracing computer program developed in this project. Each image was synthesized using 10^8 input rays.

adjusted by shift of the radiation receiving unit during visual control of the shell position by means of a mountable extensible insert (see Appendix, Sec. A.2.6). The shell shift along the optical axis leads to its displacement with respect to the observation plane. In this case, the bright-band position on the image of the shell changes.

Figure 21 presents a set of images modeled using the 3D Ray Tracing program for various positions of the equatorial plane of the shell with respect to the observation plane. Figure 22 plots a dependence of the position of the bright-band maximum versus the position of the observation plane for various apertures. Calculations have shown that a shift in the observation plane by ± 0.05 fractions of the radius of a microobject leads to a change in the bright-band position by ± 0.0015 fractions of the radius. In other words, in terms of the target 1.5 mm in diameter, the shift of the observation plane by 45 μm leads to an error in determining the position of the target's inner plane by ~ 1 μm. The zone in the plot where the bright-band position is a function of the shape and physical properties of shell's layers is marked by a rectangle. The bright-band intensity has maximum exactly at the point where the curves in Fig. 22 have a maximum. Outside this zone, the bright-band intensity sharply decreases and its width increases. The band becomes blurred, which significantly complicates the subsequent processing of the image and decreases the accuracy of determining the bright-band position. Thus, the accuracy of the optical-system adjustment to the equatorial plane of the shell largely determines the accuracy of reconstructing the shell

parameters by a set of its shadow projections.

The precise tuning was ensured by working out an adjustment technique by the outer edge of the microobject. The technique is based on the analysis of the intensity gradient in the small part of the image, which includes the shell edge. To realize this technique, we developed a special program (Sharp Edge). The program makes possible the tuning by a numerical criterion – the value of the function of the intensity gradient close to the object edge, as shown in Fig. 23a. The calculation algorithm is based on the Sobel transformation. The optical system is adjusted in real time — the operator searches for a position with the maximum intensity gradient, based on the readings of the working window of the Sharp Edge program (Fig. 23b). To rule out random noise peaks, the program provides an integral mode of calculating the maximum gradient. Practical applications of this technique have shown that the stability of the results obtained is much higher than at visual adjustment.

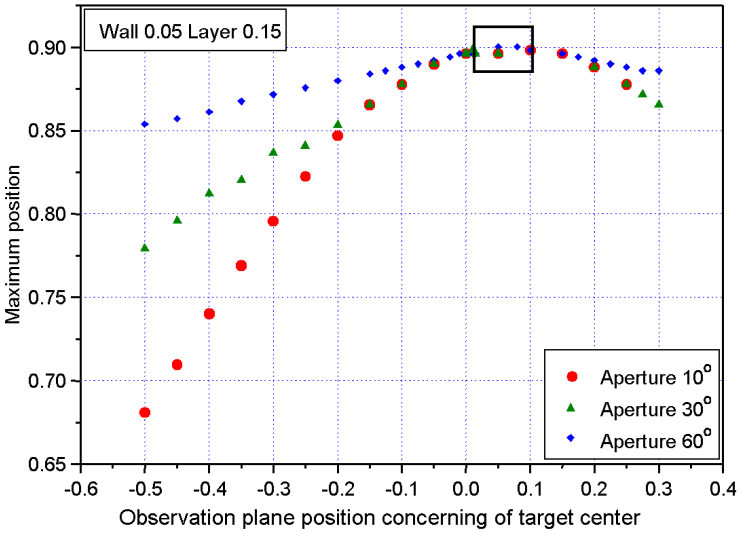

Fig. 22. Dependence of the bright-band-maximum position on the observation-plane position for various apertures (refractive index of the shell $n_1 = 1.5$, refractive index of the cryolayer $n_2 = 1.14$).

4.2. Optimization of the Observation Aperture

The effect of the observation aperture on the quality of shadow images was preliminarily analyzed on synthesized images of a cryogenic target (see Sec. 3.3.1 and Fig. 14). Comparison showed the need to choose the optimum aperture for each particular microobject. Further studies were conducted with real single-layer shells (microspheres). The observation aperture of the optical system was varied within the range from $A = 0.039$ $(2\sigma = 4.4°)$ up to $A = 0.5$ $(2\sigma = 60°)$.

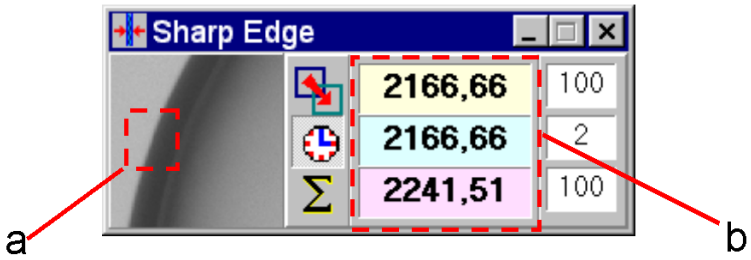

Fig. 23. Interface window of the Sharp Edge program when the study area is the microsphere edge (a) and information windows: upper – the current value of the intensity gradient, mid – the previous value of the intensity gradient, and lower – the maximum value of the intensity gradient for all measurements (b).

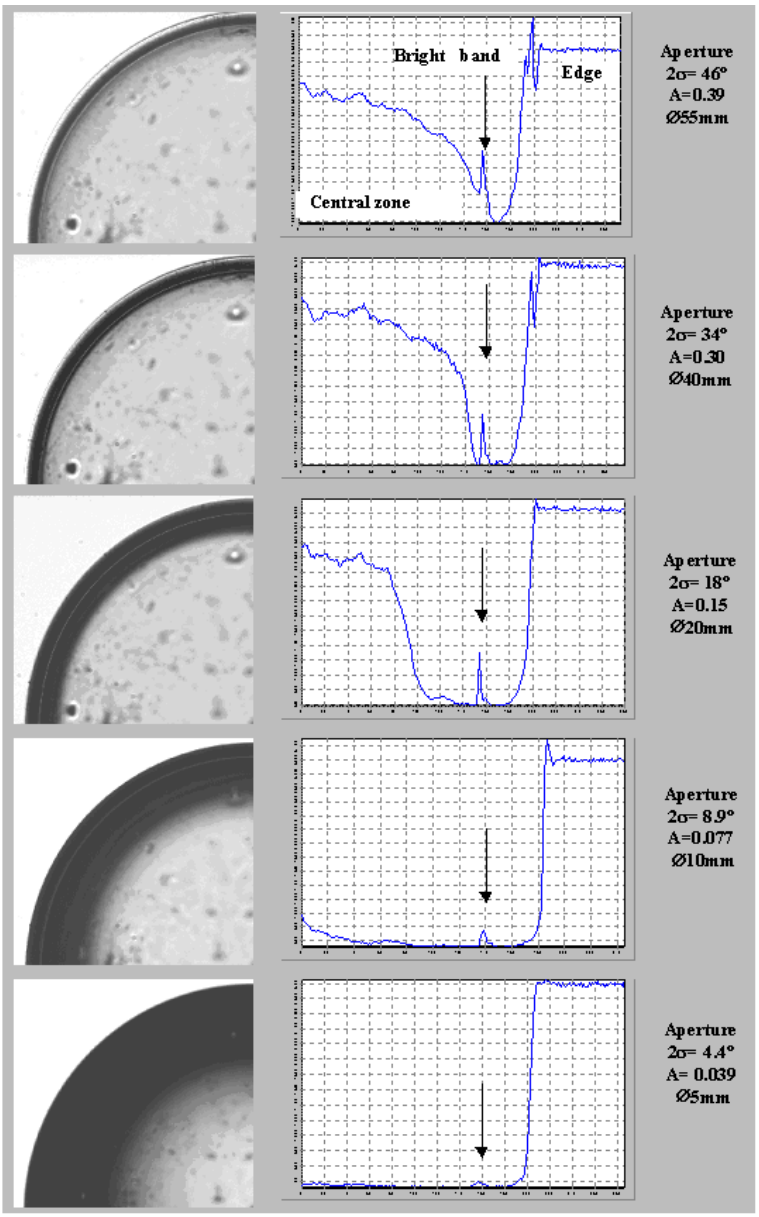

Fig. 24. Evolution of the bright-band intensity upon a change in the observation aperture. Parameters of the target: diameter 1425 μm, wall thickness 22 μm; material of the wall, polystyrene.

Figure 24 shows the shadow images and respective intensity profiles obtained for a real microsphere at various apertures. As seen in Fig. 24, a strong outburst of intensity appears in the region of the outer border of the microobject at an aperture $>30°$. This effect, due to the radiation reflection from the outer surface of the microsphere, complicates the computation processing of the image, in particular, determining the position of its outer border. At apertures $< 15°$, the brightness of the inner band becomes too small, which makes difficult the computation processing of the image and introduces an additional error into the reconstruction results. Thus, the optimum observation aperture is within the

range of ∼15–30° and should be chosen for each particular microobject separately.

4.3. Results of Reconstruction of a Transparent Microsphere from Polystyrene by a Large Number of Projections Using Target Studio Software

Since the created diagnostic complex has no analogs in the world, a paramount task was to prove the reliability of its operation and the correspondence of the reconstruction results to the required measurement accuracy. The test trials included two stages — the main stage and the demonstration stage. The following results were obtained.

1. *The main stage. Tomography of the same microsphere at two different tomographs (Shell Tester and FST Tester) with processing of a large number of projections* (>80).

At this testing stage, two sets of shadow projections of the same microsphere were created: one, when using the scanning system of the Shell Tester tomograph, and the other, on the scanning system of the FST Tester tomograph. The projection databases were formed under the following observation conditions:

- FST Tester
  - aperture number of the microscope objective $A = 0.09$;
  - number of projections $N = 81$;
  - aperture of the lighter $2\delta = 0.094$;
  - diffraction limit is 1.012 μm;
  - the position of the object plane was adjusted using the criterion of the bright-band maximum intensity.
- Shell Tester
  - aperture number of the microscope objective $A = 0.098$;
  - number of projections $N = 90$;
  - aperture of the lighter $2\delta \geq 0.1$;
  - diffraction limit is 1.553 μm;
  - the position of the object plane was adjusted using the criterion of the bright-band maximum intensity.

The databases obtained were processed using the Target Studio computer program. The processing parameters (prefiltration, contour determination of the threshold criteria, interpolation range, etc.), after their determination for the first projection, remained invariable for all the subsequent sets of projections. The reconstruction results for a microsphere by a set of projections are given in Table 4. Figures 25 and 26 present samples of the initial shadow images and a 3D visualization of the reconstruction results. As seen in Table 4, the microsphere reconstruction parameters obtained at different tomographs (Shell Tester and FST Tester) coincide to an accuracy of the measurement error, i.e., to an accuracy up to the diffraction limit preset by the image-forming mode.

2. *The demonstration stage. Measurement of the parameters of a microsphere in 1–2 projections using a traditional method and comparison of these results with the tomography data.*

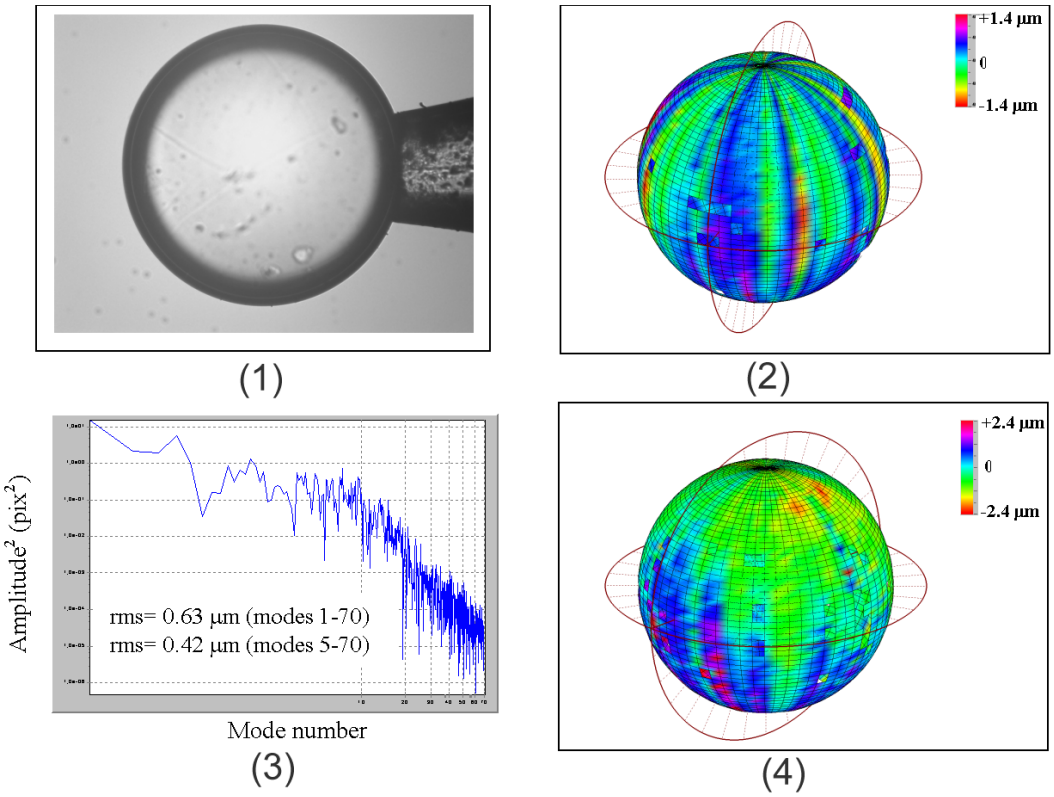

Fig. 25. Reconstruction of a polystyrene microsphere using a database (90 shadow projections) formed on a Shell Tester tomograph: shadow projection of the microsphere (1), outer surface of the microsphere (reconstruction) (2), Fourier spectrum of the bright band (3), and inner surface of the microsphere (reconstruction) (4). Reconstruction was performed using the Target Studio software (see Table 4 for the reconstruction parameters).

As an example, Fig. 27 shows images of the same polystyrene microsphere obtained by different methods — using a Shell Tester tomograph, Jamin interferometer, MIR-3 X-ray microscope, and also an image of a microsphere in an immersion liquid (glycerine).

The following measurements were made at the second stage:

- *Measurements of the microsphere-wall thickness by its interferogram obtained using a Jamin interferometer.*

  The shell thickness was determined as the mean of arithmetic measurements by five pairs of interference rings in the image, according to the formula

$$d = \frac{\lambda}{2}\left[(n^2 - x_2^2)^{1/2} - (n^2 - x_1^2)^{1/2} - (1 - x_2^2)^{1/2} + (1 - x_1^2)^{1/2}\right]^{-1}, \qquad (15)$$

  where x_1 and x_2 are the diameters of the neighboring interference rings; herewith, x_2 is the diameter of the larger ring and x_1 is the diameter of the smaller ring.

- *Measurements of the wall thickness of a microsphere placed in an immersion liquid.*

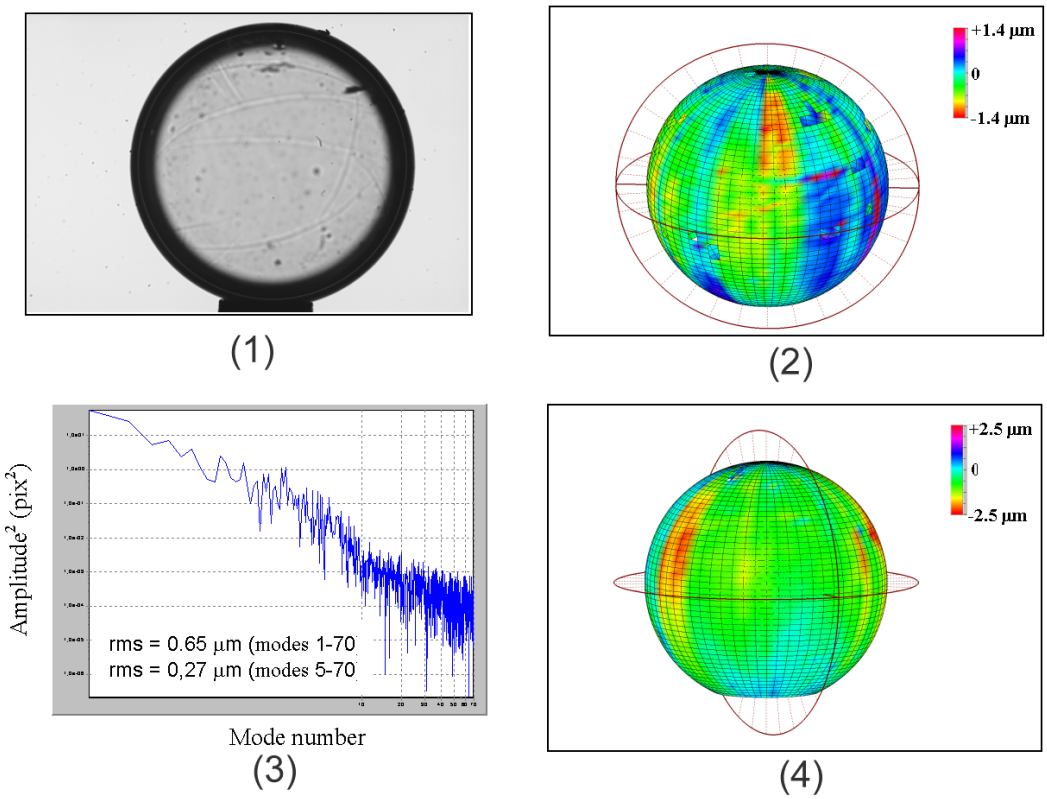

Fig. 26. Reconstruction of a polystyrene microsphere using a database (90 shadow projections) formed on a FST Tester tomograph: shadow projection of the microsphere (1), outer surface of the microsphere (reconstruction) (2), Fourier spectrum of the bright band (3), and inner surface of the microsphere (reconstruction) (4). Reconstruction was performed using the Target Studio software (see Table 4 for the reconstruction parameters).

The measurements were carried out for 8 radial cross sections evenly distributed along the perimeter of the shadow image of a microsphere in an immersion liquid. The immersion liquid was glycerine, which is inert with respect to the material of the microobject. The refractive index of glycerine in the visible spectrum $n = 1.47$, which is sufficiently close to the refractive index for polystyrene ($n = 1.58$).

- *Measurement of the outer diameter and thickness of a microsphere using an IMTsL-100×50 commercial metallographic microscope.*

  The measurement of the outer diameter of the shells was carried out for 30 projections. In each projection, the measurements were done in 5 noncoinciding directions. The measurements were fixed by a UtsO-201S standard digital counter with a measuring step of 0.2 μm. A 10× objective lens with a digital aperture of 0.2 was used in order to increase the spatial resolution. The error limit of the counter at a length of 1500 μm was ± 0.5 μm.

  The measurements carried out at the second stage of the tests showed the following:

- Value of the outer radius of the microsphere, μm

Table 4. Reconstruction of the Parameters of a Microshell Using Tomographs.

Microshell parameters		Units	Results		
			FST Tester	Shell Tester	Discrepancy
Outer radius	Average	μm	712.4	713.5	1.1
	Minimum	μm	710.3	710.8	0.5
	Maximum	μm	716.7	716.3	0.4
	Nonsphericity	%	0.4	0.4	0.0
Inner radius	Average	μm	690.9	690.3	0.6
	Minimum	μm	687.3	684.8	2.5
	Maximum	μm	694.1	695.8	1.7
	Nonsphericity	%	0.5	0.8	0.3
Wall	Average thickness	μm	21.5	23.3	1.8
	Minimum	μm	17.7	17.2	0.5
	Maximum	μm	25.6	28.1	2.5
	Thickness variation	%	19.0	24.5	5.5

Average 711.9,
Minimum 710.0,
Maximum 714.2.

- Nonsphericity of the outer surface 0.29%,
- Wall thickness (mean of five measurements)

  by the interferogram 22.0±2.5 μm,
  microsphere in an immersion liquid 20.8±0.8 μm.

So the results of the demonstration measurements, within the error limits, coincided with the tomography results (cf. data of Table 4).

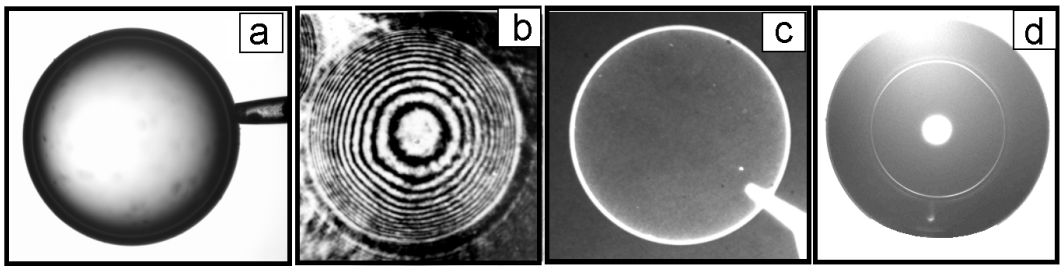

Fig. 27. Microsphere images obtained on a Shell Tester tomograph (a), Jamin interferometer (b), and MIR-3 X-ray microscope (c and d). An image of a microsphere was placed in an immersion liquid.

Thus, the tests have shown that the created diagnostic complex makes possible reliable and highly precise measurements of the parameters of ICF microobjects, such as transparent microspheres and cryogenic targets, by the method of tomography. As a result of tests on a prototype, we have first performed a 3D reconstruction of the inner surface of transparent polystyrene microspheres by a large number of shadow projections (from 80 up to 90), obtained in the visible spectral range. Herewith, the tomography of both mounted and free-standing microspheres was made. The reconstruction accuracy for microspheres 1 mm in diameter is ∼1.5 μm for the Shell Tester tomograph and ∼1 μm for the FST Tester tomograph.

5. Summary

Concluding, we summarize our main results.

- A direct algorithm and corresponding software (3D Ray Tracing, Shell Optics Model) for modeling the shadow image of microspheres and cryogenic targets were developed. Comparison of numerically obtained shadow images with the images of real microspheres confirmed the adequacy of the model created.
- An inverse algorithm for the spatial reconstruction of the inner structure of microspheres and cryogenic targets by the bright-band position at the shadow projections of these microobjects (the so-called BBP algorithm) was developed. The results of numerical experiments to test the algorithm showed that the mean deviation of the reconstruction results from the test target parameters does not exceed 1%.
- A diagnostic complex (a multi-projection tomograph) consisting of an original scanning system and specially developed software Target Studio was created. The complex comprises two different tomographs, including the Shell Tester tomograph intended for operation with mounted microspheres at room temperature and the FST tomograph enabling work with free-standing microobjects (microspheres and cryogenic targets) at room and cryogenic (4.2–77 K) temperatures of the microobject.

  A series of test trials was carried out, which showed the given complex to possess unique operational parameters:

Temperature of microobject	room and cryogenic (77–4.2 K);
Probing radiation wavelength	475±15 nm and 490±7 nm;
Total microobject scanning angle	360°;
Accuracy of positioning	± (1.5–2.5) arcmin;
Current number of projections	100;
Spatial resolution in the first projection	1–1.5 μm;
Diameter of microobject studied, maximum	1.5 mm;
Accuracy of reconstruction	1–1.5 μm.

  The complex enables reconstructing the parameters of a microobject transparent in the visible range of radiation, including a microobject fabricated from a material with small Z (for instance, the fuel layer inside the cryogenic target), the diagnostics of which is impossible by the method of the generally used X-ray tomography.

- 3D reconstruction of the inner structure of transparent polystyrene microspheres by a large number of shadow projections (over 80), generated in the visual spectral range, was first performed. Herewith, the tomography of both mounted and unmounted (free-standing) microspheres was realized. The results of the reconstruction of the same polystyrene microsphere at two different tomographs, which comprise the diagnostic complex, have shown that the parameter-reconstruction accuracy (for microspheres 1 mm in diameter) is ∼1.5 μm for the Shell Tester tomograph and ∼1 μm for the FST Tester tomograph.

Thus, within the framework of the chosen technological approach, we have demonstrated the possibility of efficiently solving one of the essential problems of the technology of laser targets — to perform unambiguous reconstruction of their parameters with high accuracy. The created complex provides the required sequence of diagnostics of the cryogenic target parameters, namely,

- Stage 1 – tomography of a hollow microsphere (performed at the Shell Tester tomograph);
- Stage 2 – tomography of the cryogenic fuel layer formed at the inner surface of a microsphere, the parameters of which were determined at stage 1 (performed at the FST Tester tomograph).

The results obtained can be primarily used in experimental research in ICF, in formation and delivery of cryogenic fuel targets, and also in organizing a production process at future ICF reactors. At present, the created diagnostic complex (the tomograph components and software) completes the original installation for fabrication of free-standing cryogenic targets [15] at the P. N. Lebedev Physical Institute. Specialized software developed in this work is also used at the Institute of Laser Engineering, Osaka University (Japan) for measuring the characteristics of polymer microspheres [16]. Recently the optical-tomography characterization of ICF cryogenic targets was also reported in [20].

Appendix. Description and Technical Specifications of the Main Components of the Diagnostic Complex

A.1. Shell Tester Tomograph. Diagnostics of a Mounted Microsphere

The Shell Tester tomograph is intended for measuring hollow microspheres pneumatically fixed on a glass capillary and at room temperature. After the diagnostics of its parameters, a microsphere can be used for preparing a cryogenic target (filling with fuel gas, formation of the cryogenic layer).

The general view of the tomograph is shown in Fig. 20a. The main components of the setup are described below.

A.1.1. Optical Observation System

The system of optical observation is based on an IMTsL 100×50 commercial microscope. The technical specifications of the microscope are as follows:

- range of displacements of the coordinate table:

  in the longitudinal direction 0–100 mm;
  in the transversal direction 0–50 mm;

- linear field of the microscope 21, 7, 4.2, and 2.1 mm for the range of objectives ×1, ×3, ×5, ×10, respectively;
- measurement error limit, using a digital reading device (based on 100 mm) ±3 μm.

The microscope makes use of a custom-made OVS-1 fiber-optics lighter with a broad-band thermal source of radiation (an incandescent lamp with color temperature of 2500–3000 K) and a condenser. The lighter's power is supplied from the ac mains via a stabilizing transformer. A specially fabricated bandpass light filter with the bandpass maximum at a wavelength λ=490 nm and quality factor $\lambda_0/\delta\lambda$=70 is used to form the working spectral range of the probing radiation.

The spatial instability of illuminance in the work field is ∼6%, being mainly determined by the characteristics of the microscope's condenser. The temporal instability of radiation is several times lower than the level of intrinsic noise of the radiation receiver. One of two different CCD cameras – Cool Snap or SenSys 3200 (Photometrics) – is used as a radiation photoreceiver. The technical specifications of the cameras are given in Table 5. The SenSys CCD camera has a larger number of active elements than the Cool Snap camera, which makes it possible to increase the field of vision in the object field ≈1.5 fold. Moreover, vision in the object field ≈1.5-fold and the Kodak higher-quality image is due to the 3-fold decrease in the digitation noise. Studies of the spatial resolution of the optical system were carried out using two types of test objects:

- standard test object pattern with distance between the 25th field lines equal to 5 μm;
- UV-memory chip fabricated by microtechnology with a characteristic distance between the elements (lanes) of ∼1.5 μm.

Table 5. Technical Specifications of CCD Cameras.

Parameters and type of camera	Cool Snap	Sen Sys 3200
Type of CCD matrix	Sony ICX285	Kodak KAE3200E
Matrix format:		
- number of pixels	1392×1040	2184×1472
- pixel size, μm	6.45×6.45	6.8×6.8
- light-sensitive area, mm	8.77×6.6	14.8×10.0
Nonlinearity	<1%	≤0.5%
Temperature stabilization	yes	yes

Analysis of the images obtained showed that the ultimate resolution of the microscope's optical system is at the level of 1.2 μm (for a ×10 objective). Herewith, the image contrast was 10–12%.

The aim of characterizing a microsphere is to obtain with high accuracy the parameters of its outer- and inner-surface and wall-thickness variation, proceeding from a set of shadow projections (images). Information on the conversion coefficient K is required to determine the absolute values of the parameters. The conversion coefficient is defined as the ratio of the size of the object in micrometers to the size of its image in pixels. To determine the conversion coefficient, we used a calibration scale with a grid

step of 0.01 mm and a field of 1 mm (the set OMP No. 650286 similar to the Russian State Standard GOST 7513-55). The sought-for conversion coefficient for the coordinates of the objective of a microscope with a 3-fold magnification was $K = 1.5525$ μm/pixels $\pm 0.01\%$. The root-mean-square deviation of the size of the calibration scale was ± 0.054 pixels.

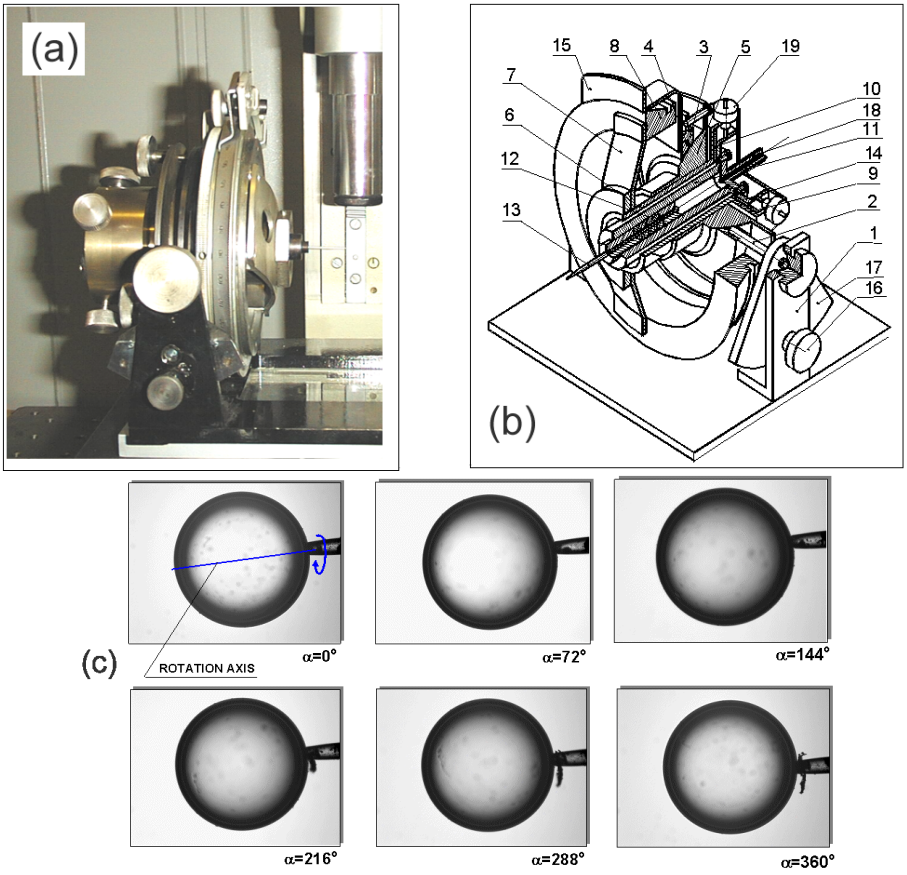

Fig. 28. A microobject positioner in the Shell Tester tomograph: general view (a), schematic: support (1), screw (2), ring (3), ball-and-socket joint (4), flange (5), sleeve (6), arm (7), limb (8), cup (9), magnet (10), tube (11), sleeve (12), capillary (13), bowl (14), ruler (15), stopper (16), sector (17), connector (18), and micrometer screw (19) (b), and a series of projections of a polystyrene microsphere with outer radius 1676 μm, wall thickness 43 μm, and glass capillary diameter 44 μm (c). Scanning conditions: number of projections 100, angle increment $3.6° \pm 1.5$ arcmin.

A.1.2. Microsphere Positioning Device

The schematic and general view of the angular positioning device are shown in Fig. 28. The target is rotated with respect to the horizontal axis. Capillary (13) on which the target is held pneumatically due to the vacuum pumping of the inner volume of the capillary through connector (18) is used as a support. The diameter of the capillary tip is from 40 up to 100 μm. To prevent damage to the target's outer surface, the edges of the tip are fused off. A feature of the device is the possibility of aligning the axis of rotation of the microsphere and its center by means of micrometer screws (19). The angular position of the microsphere can be read by limb (8) and vernier ruler (15). The surface of the target in the polar

zones located on the axis of rotation can be monitored by turning the whole angular positioning device with respect to screw (2). This makes possible target scanning in the plane located at angles of 10°, 20°, and 30° with respect to the horizon. Rotation of the target is even at a total scanning angle of 360°.

The technical parameters of the positioning device are:

1. Linear displacements of the microsphere
   - along the capillary axis — 100 mm;
   - in the vertical direction — 50 mm;
   - accuracy of displacement — 1 μm;
2. Angular displacements of the microsphere
   - with respect to the capillary axis — ±180°;
   - tilt with respect to the axis of rotation — ±10°, ±20°, ±30°;
3. Accuracy of determining the rotation angle — ±1.5 arcmin;
4. Number of steps at a turn to 360°, maximum — 1000;
5. Diameter of the target — < 2000 μm;
6. Diameter of the capillary tip — 40–400 μm.

A.2. FST Tester Tomograph: Diagnostics of a Free-Standing Target

The FST Tester is intended for the diagnostics of free-standing cryogenic targets at temperatures of 20–4.2 K. If required, this tomograph can also be used for the diagnostics of free-standing hollow microspheres (at $T = 300$ K or 77–4.2 K).

The component composition of the tomograph and its optical schematic are shown in Fig. 29 (a and b), and the general view of the setup is shown in Fig. 20b. All components are arranged on the standard preumatic-vibration-isolated optical table Standa 1VIS95W, which provides efficient shock absorption of high-frequency resonance vibrations up to frequencies of 1 GHz. A description of the main components of the setup is given below.

A.2.1. Radiation Source (Lighter)

A narrow-band luminescent diode U-266S (Fig. 29, 1) is used as a source of radiation in the lighter. At the output of the luminescent diode, there is diffusing ground glass (Fig. 29, 2), which improves the spatial uniformity of radiation. Technical specifications of the luminescent diode:

- radiation power — 30–45 mW;
- light intensity — 4–6 cd;
- spectral range (maximum radiation intensity) — 465–475 nm;
- divergence of radiation (half angle) — 40±5°;
- rated/maximum direct current — 350/400 mA.

The luminescent diode is fed by a B5-45A laboratory power supply, which provides stability of the output current at the level of ±0.1%. The field stop (field iris diaphragm) (Fig. 29, 3) determines the value of radiation divergence and power at the output of the radiation source (lighter). To reduce the radiation-intensity losses, the luminescent diode, ground glass, and field stop are located at the minimum

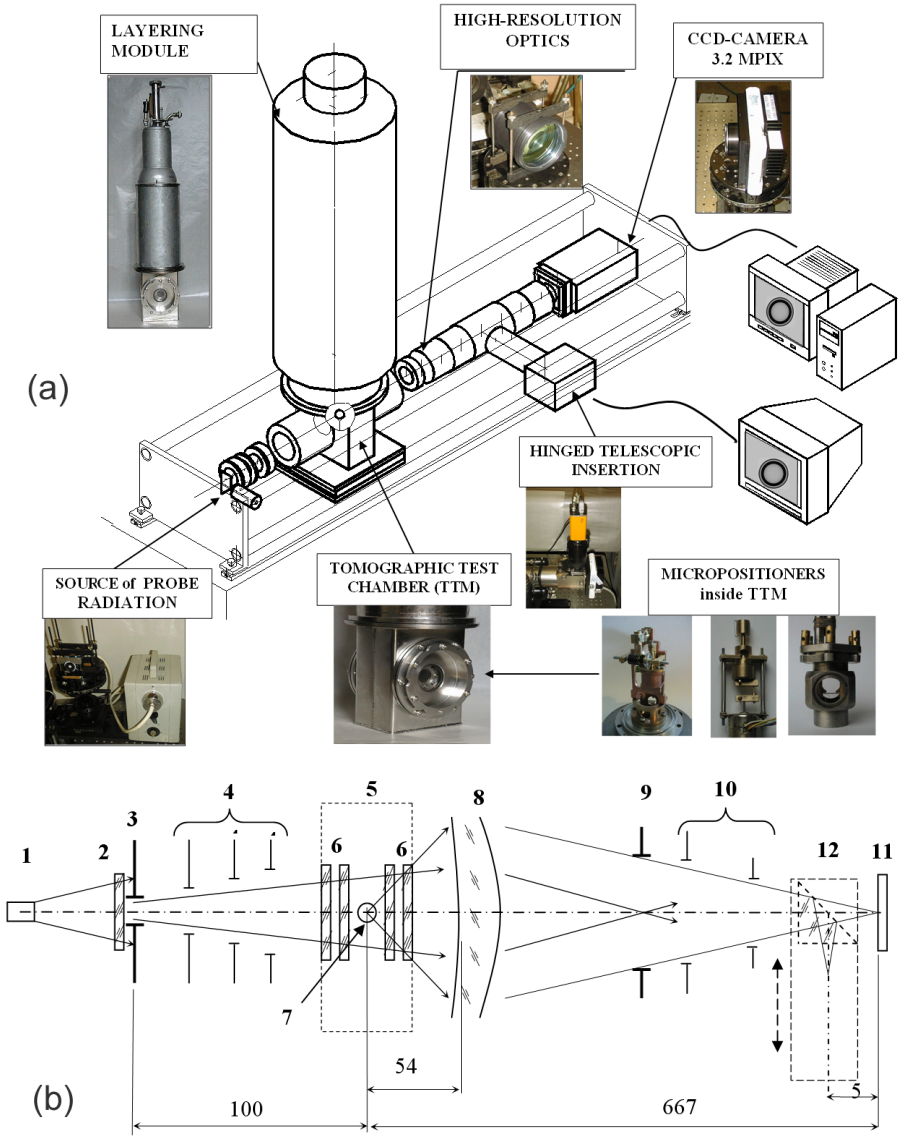

Fig. 29. FST Tester tomograph: isometric view of the main components (a) and optical schematic: radiation source (lighter) (1), ground glass (2), field iris diaphragm 0–12 mm in diameter (3), tomographic test chamber (4), protective windows of the cryostat (6), microobject (cryogenic target) on the positioning device (7), microlens with $6.5^{\times}$ and $A = 0.5$ (8), aperture iris diaphragm 5–75 mm in diameter (9), shade diaphragms (10), CCD camera (11), and mounted insert (12) (b).

admissible distances one from the other. All components are mounted in one body, which is placed on the adjustment table. The intensity and uniformity of illumination were studied after the position of the lighter was adjusted with respect to the microobjective lens. During the adjustment, the object field was photographed by the CCD camera with exposure time of 0.01 s. Since the exposure of modes can reach 1–2 s, the margin of exposure time (illuminance of the microobject) is 1–2 orders of magnitude.

To check the uniformity of illumination, we studied the illuminance of the object field for three different positions of the CCD matrix (the matrix turn in the plane perpendicular to the optical axis by 0°, +90°, and +180°). Herewith, the image of the radiation source was projected through the microobjective lens to the center of the aperture diaphragm, and the center of the light field coincided with the center of the input lens of the microobjective.

Analysis of the images obtained showed:

- the absolute nonuniformity of intensity (by the diagonal cross sections) is ∼20 units of AD converter amplitude, which corresponds to a relative nonuniformity of ±0.4% at an average level of illumination of 3930 ADC units;
- the nonuniformity of illumination is a consequence of the nonuniform sensitivity of the CCD matrix elements, i.e., upon a change in position of the camera the nonuniformity pattern did not change with respect to the matrix coordinates.

The obtained results demonstrated that the quality of the radiation source satisfies the technical requirements (see Sec. 3.4). The nonuniformity of illumination is at a level of the intrinsic noise of the CCD matrix and can be disregarded when using the BBP reconstruction algorithm.

Technical parameters of the radiation source:

- radiation source	blue luminescent diode U-266S;
- diameter of the iris diaphragm	0–12 mm;
- distance from the diaphragm to the target	280 mm;
- working field in the plane of the target	1.5–2.0 mm;
- uniformity along the working field	±0.4%;
- adjustment range of the radiation divergence 2δ at a target ∅ 1 mm	0.1–1.3°.

A.2.2. Test Tomographic Chamber

The test tomographic chamber (TTC) is intended for optical studies of a microobject (microspheres or cryogenic targets) in the scanning mode. For this purpose, a special dynamically-positioning device with the microobject is installed inside the chamber, using which the microobject is rotated in the process of scanning. The chamber is mounted in the lower part of the standard KG-20 cryostat and provides an aperture observation angle of 63° (maximum) at a distance of 54 mm from the microobject to the outer surface of the microobjective lens. The dimensions of the inner volume of the TTC are 7×5×8 cm. The general view of the TTC and the schematic of the arrangement of the positioning device inside it are shown in Fig. 30.

The inner part of the TTC represents a helium chamber (HC), which is attached to the shaft of the cryostat. The HC walls are cooled with helium, which is passed along the serpentine-shaped heat exchanger. There are optical windows at the opposite side walls of the chamber. From the bottom, the HC is hermetically sealed by a removable flange, on which the positioning device (PD) is mounted, and a sealed electrical input for connecting the power supply for the PD step motor and tapping the data from the temperature pickups. The HC is enclosed with a nitrogen shield to reduce the infiltration heat of the radiation from the outer casing, which is at room temperature. The shield is equipped with two windows coaxial with the HC windows.

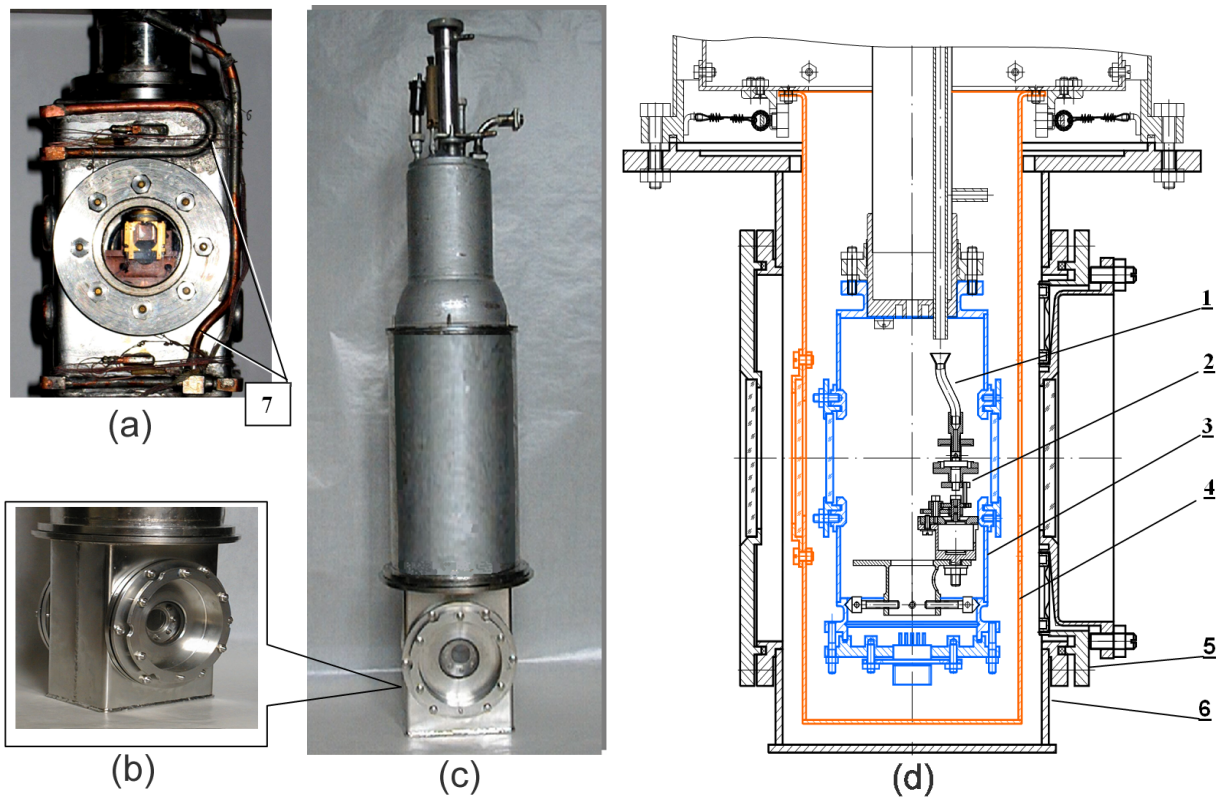

Fig. 30. Tomographic test chamber (TTC): helium chamber (a), general view (b), KG-20 cryostat (c), and schematic location of the PD-1-type positioner: target loading (1), PD-1 (2), helium chamber (4.2–20 K) (3), nitrogen shield (77 K) (4), flange for fixing the movable window (5), outer casing (300 K) (6), and serpentine-shaped helium heat exchanger (7) (d).

The TTC outer casing, which is a continuation of the cryostat body, is outside the nitrogen shield. There are two windows in the casing, which are coaxial with the HC and nitrogen-shield windows. One of the windows is stationary; the other (on the side of the objective lens) is fixed using a movable membrane and makes possible adjustments to provide the flatness of the windows. The TTC makes it possible to study a microobject at temperatures of 77–4.2 K, as well as at room temperature (without filling the cryostat with coolants). The temperature on the surface of the helium chamber is controlled by two DT-470 semiconductor thermometers. Tests of the TTC at room and cryogenic temperatures confirmed that the parameters of the chamber satisfy the technical requirements.

A.2.3. Microobject Dynamically-Positioning Device

The dynamically-positioning device (PD) is one of the key elements of the scanning system in the FST Tester tomograph. This device is inside the tomographic test chamber of the cryostat and, therefore, should be sufficiently small (to fit the inner volume of the TTC, 7×5×8 cm) and provide the dynamic mode of getting the required projections in operation with a free-standing microsphere and cryogenic

target, including at cryogenic temperatures. The unique requirements imposed on the PD called for an original device to be worked out. It was developed in three modifications. The technical characteristics of the devices are given below.

A.2.3.1. PD-1 Device with Constant Vertical Axis of Rotation

The schematic diagram and general view of the PD-1 are given in Fig. 31b, and the schematic of its arrangement inside the TTC is shown in Fig. 30d. The peculiar features of the device are as follows.

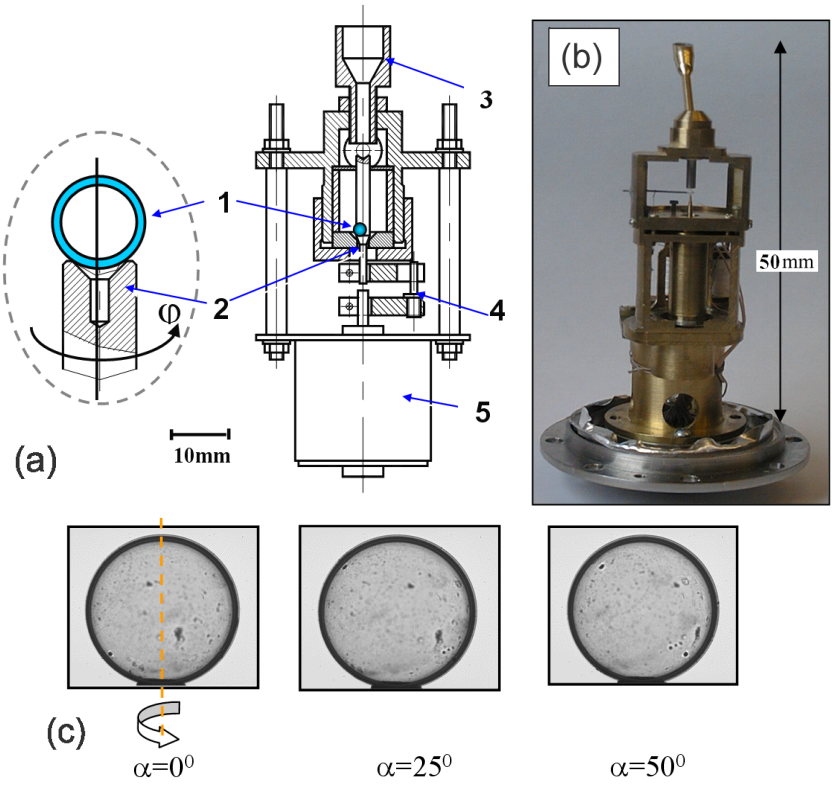

Fig. 31. PD-1-type positioning device: schematic diagram of the device detailing the target position on the bearing cone: cryogenic target or microsphere (1), shaft (2), target loading unit (3), reducing gear (4), step motor (5) (a), general view of PD-1 mounted on the fixing flange in the TTC (b), and examples of shadow images (c).

A free-standing cryogenic target or a hollow microsphere, through the target loading channel (Fig. 31a, 1), is fed from the cryogenic channel into the tapered socket of the support shaft. In the process of scanning, the target is rotated together with the shaft with respect to the vertical axis. A standard DShR20-18-00 bidirectional step motor is used as a rotation drive (minimum angle step 18°, systematic step error ±5%). The motor is mounted in the lower flange of the TTC. The rotation from the motor to the support shaft is transferred by means of a step-down gear with a reduction coefficient of 72. Figure 30c shows a number of projections of a polystyrene microsphere obtained at the rotation of the PD-1. An advantage of the PD-1 is the simplicity and reliability of construction; a disadvantage is the presence of two 'shadow' zones on the surface of the microobject, which is a consequence of its rotation

with respect to the invariable vertical axis.

The working characteristics of the PD-1 make it possible to realize the following scanning conditions (irrespective of the target diameter):

- Complete scanning angle 360°;
- Maximum number of projections 144;
- Step increment 2.5°;
- Positioning accuracy 1.6 arcmin.

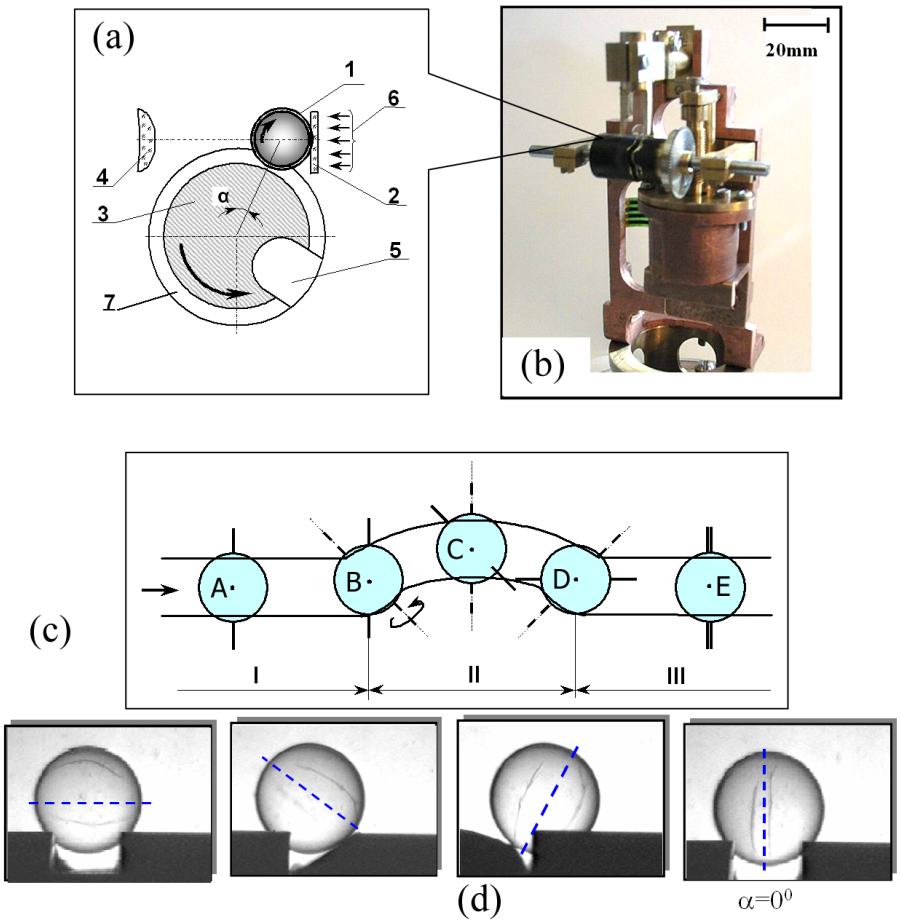

Fig. 32. PD-2 positioning device: schematic diagram with target (1), glass plate (2), support shaft (3), objective lens of the microscope (4), chamfer for removing the target (5), backlighting (6), and guiding groove (7) (a), general view (b), schematic of the movement of a microsphere with the change of the rotation axis in the guiding groove (c), and movement of a real microsphere with the change of the rotation axis (d).

A.2.3.2. PD-2 Device with Variable Axis of Target Rotation

In the variant of the PD-2, the target is rotated both with respect to the radiation and the support shaft. This provides a possibility to exclude the shadow zone in scanning the targets due to the change in the rotation axis. The schematic diagram and general view of the positioner are shown in Fig. 32a and

b. In the process of operation, a free-standing target (1), through the target loading channel, is fed to the shaft (3) and is fixed in the scanning plane by means of the limiting glass plate (2). Displacements of the target along the support-shaft axis are limited by the groove (7) made by the cylindrical-surface perimeter. When the shaft rotates, the target moves along the groove due to the forces of friction between the target and the surface of the shaft.

To change the target-rotation axis, the groove of the shaft has a turning sector, passing which, the target begins to rotate around another axis turned by 90° with respect to the initial axis, as shown in Fig. 32c (in the unfolding to the plane). In region I, the target rotates around the axis parallel to the shaft axis. Starting from point B and up to point D, the target rotates around another axis, which makes an angle of 45° with the initial axis. In point D, the rotation axis again changes by 45°. As a result, in region III the target-rotation axis appears perpendicular to the initial axis. Thus, the zones of the target, which were 'polar' in region I, become 'equatorial' in region III. In this way, it appears possible to avoid dark zones on the target surface during its scanning (see Fig. 32d).

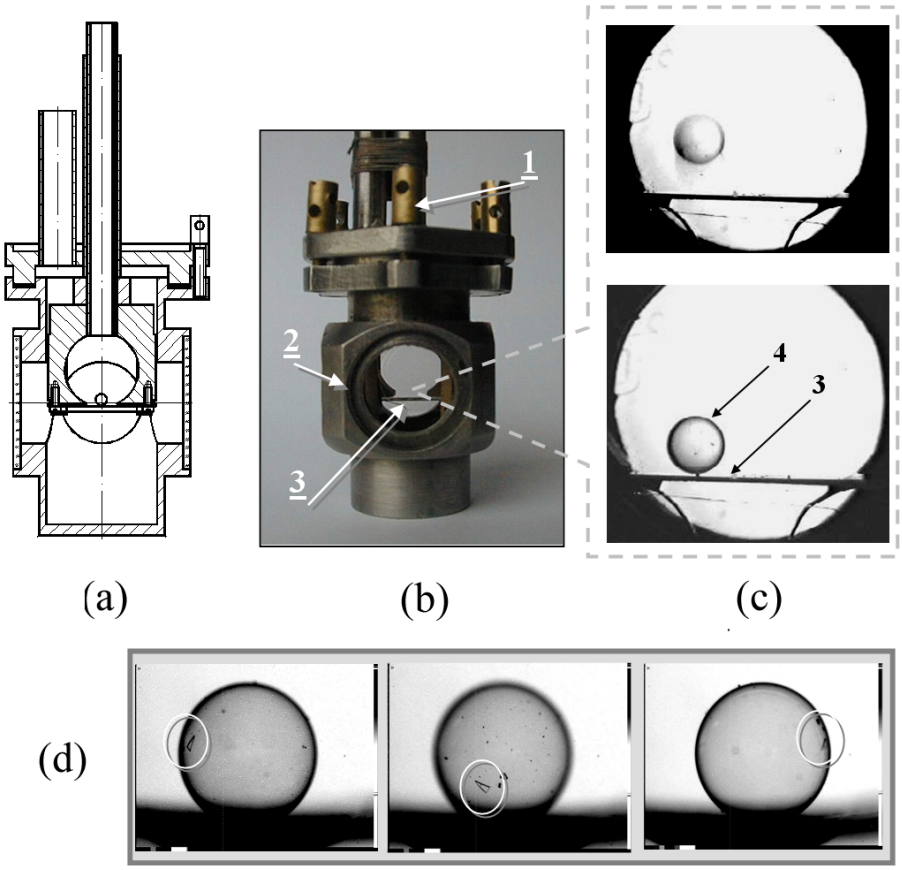

Fig. 33. Rotating and bouncing (R & B) cell: schematic diagram with tube for loading cryogenic targets (1), chamber (2), target (3), and piezocrystal (4) (a), helium chamber assembled with R & B cell (b), a target in the bouncing mode on a piezocrystal (c), and a target in the rotation mode (d).

Upon scanning, the target is evacuated through a special hole (Fig. 32a, 5). It goes down the hole to

vacate the space for the next target. The same step motor and the same control unit as for the PD-1 model is used as the rotation drive. The rotation from the motor to the support shaft is transferred by means of a step-down gear of the worm type with a reduction coefficient of 72. Tests of the PD-2 at room and cryogenic temperatures (77–4.2 K) have confirmed that the device satisfies the technical requirements. The working characteristics of the PD-2 permit one to realize the following scanning conditions (for a target of 1.5 mm in diameter):

- Complete scanning angle 360° (for the first scanning direction);
- Maximum number of projections 144 (for the first axis of rotation);
- Step increment 1.3°;
- Positioning accuracy 4 arcmin.

A.2.3.3. R&B Cell with Random Turning Angle

The general view of the R&B (rotating and bouncing) cell is shown in Fig. 33. The device represents a vacuum optical chamber, inside which there is a piezocrystal in the form of a plate with fixed ends. The displacement of a free-standing microsphere or a cryogenic target with respect to the crystal surface is realized by feeding the crystal with a current of preset amplitude and frequency. The power supply of the R&B cell is controlled by a standard G6-34 multifunctional generator, which provides operation with rectangular voltage pulses within the range of 0.5–75 V and frequency range of 10^{-3}–10^{6} Hz. Tests of the device at cryogenic temperatures (4.2–77 K) demonstrated the possibility (depending on the piezocrystal vibration frequency) of changing the amplitude of the target displacement with respect to the support within a wide range – from rotation at a minimum angular rate to bounces of the target with respect to the support to a height of 2 up to 10 target diameters. Figure 34 shows the dependence of the target-displacement amplitude on the control pulse frequency obtained at $T = 4.2$ K.

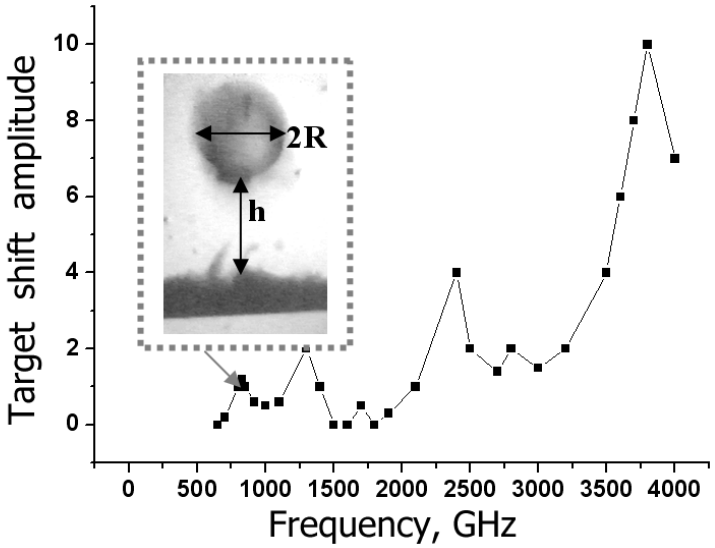

Fig. 34. Travel amplitude $A = h/2R$ (h is the height of the target lift and R is the target radius of a shell with a diameter of 2 mm) in the R & B cell as a function of the drive pulse frequency.

A.2.4. Microobjective Lens

The microobjective lens provides the formation of the microobject image on the CCD matrix. The requirements imposed on the microobjective (resolution ∼1 μm, a considerable front part ∼55 mm at a high angular aperture ∼60°) necessitated the development of an original device. The general view of the device is shown in Fig. 35.

The microobjective is designed for a working wavelength of 490±7 μm. In the process of fabrication, its

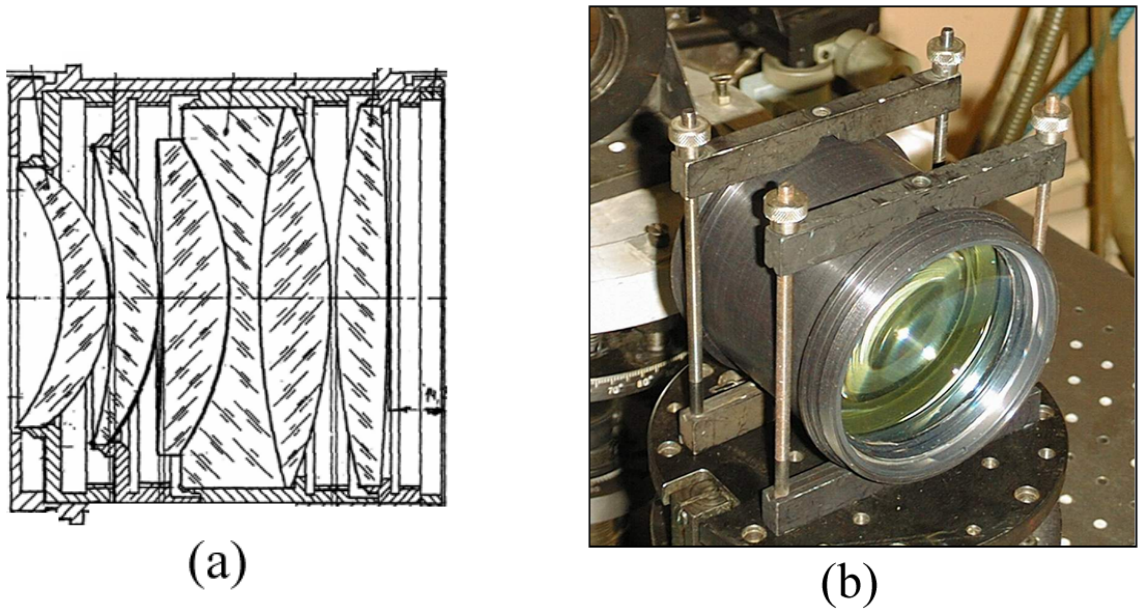

Fig. 35. High-resolution microobjective lens: assembly drawing (a) and general view (b).

design was amended to take into account the characteristics of the glass used (colorless optical glass, grade K-8). A special testing technique was developed for testing the resolving power of the microobjective. The resolving power was determined by observing an image of a moiré test pattern. In accordance with the testing protocol (see Fig. 36), the projection objective lens (4) creates an image of the test pattern (3) reduced 40 times. This image is transferred through the microobjective (5) into its image plane at a magnification of 6.5×. The final image is seen by an observer through the microscope (6) at a magnification of ≈100×.

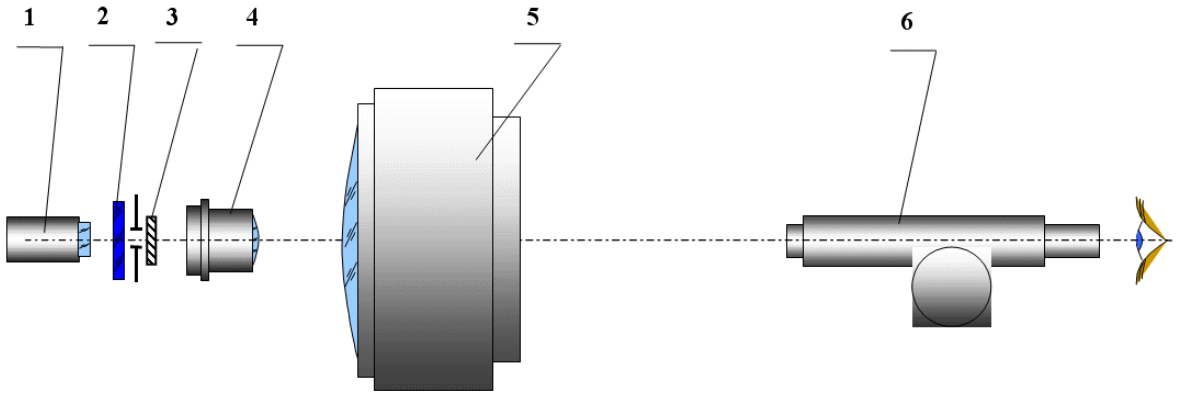

Fig. 36. Optical schematic for checking the resolving power of the objective lens: lighting system (1), light filter for $\lambda \cong 0.49$ μm (2), test chart (3), projection lens with magnification $\beta = -40$ and aperture $A = 0.65$ (4), tested microobjective lens (5), and microscope with magnification ∼100× (6).

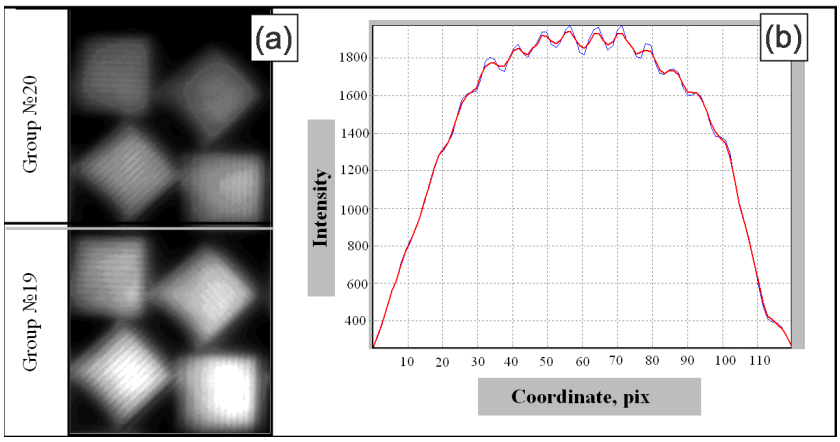

Fig. 37. Results of testing the objective lens: image of test chart groups 19 (1400 lines/mm) and 20 (1600 lines/mm) (a) and intensity record for 2 elements of group 20 (b).

Out of two fabricated 6×0.5 microobjectives, the tests revealed the best specimen (with the maximum spatial resolution). The test results have shown that the spatial resolution of the chosen microobjective corresponds to values of 1400–1600 lines/mm or 0.6–0.7 μm, which is close to the diffraction limit. Herewith, the image contrast is 5–7%, which ensures reliable processing of the image (Fig. 37).

If the coefficient of conjugation of the microobjective and the CCD camera is unity (1 μm of an object is projected on 1 pixel of the camera), then the physical resolution of the image obtained using the receiving unit is 1 μm. By changing the conjugation coefficient two times, the resolution can correspondingly increase. Analysis of the moiré test pattern images obtained for the wavelength range ($\lambda = 475\pm15$ μm) shifted with respect to the nominal range ($\lambda = 490\pm7$ μm) showed that, for the same group of elements of the reference moiré test pattern, the changes in the spatial resolution and spherical aberrations are small and within the limits of the measurement error. The result obtained demonstrated the possibility of using the objective in a shorter wavelength region of the spectrum. This made it possible to exclude the light filter from the optical setup, which simplified the design of the lighter and provided a larger uniformity of illuminance in the object plane.

The technical specifications of the created microobjective are:

- Working wavelength 490±7 nm;
- Numerical aperture 0.5;
- Magnification 6.5;
- Calculated field of vision 1.5 mm;
- Spatial resolution (not worse than) 1.0 μm;
- Depth of focus ∼1 μm.

A.2.5. Radiation Receiver (CCD Camera)

A standard monochromic CCD camera of the SenSys 3200 type with the CCD matrix science grade 0 was chosen for recording. The general view of the receiver and its arrangement in the tomograph setup are shown in Fig. 29a. The CCD matrix has a sensitivity maximum in the spectral range of 470–490 nm with quantum efficiency of ∼50%. Thermal stabilization of the matrix at the level of 10°C makes it

possible to reduce significantly the noise component of the signal. The total dynamical range is 12 bit at a digitation rate of 1.4 MHz. The device for fixing the camera to the optical accessories of the tomograph provides the complete set of displacements during the adjustment. The test experiments confirmed the operational parameters of the camera given in Table 5. At the total dynamic range of 4096 counts of the ADC, the noise component did not exceed 10–20 ADC units, which ensures reliable and highly precise information in the processing of an image.

Determination of the absolute values of the reconstructed parameters of a microobject requires information on the coefficient of conversion of the CCD matrix coordinates into the linear coordinates of an image. This coefficient is defined as the ratio of the size of the object in micrometers to the size of its image in pixels. As a result, the coordinate conversion coefficient was $K = 1.0120$ μm/pixels$\pm$0.02%. The root-mean-square deviation of the size of the calibration scale was ± 0.16 pixels. The measurements were carried out at room temperature, at the completely assembled FST Tester. The calibration scale was placed inside the test tomographic chamber.

A.2.6. Mountable Expandable Insert

The mountable expandable insert (see the schematic in Fig. 29a) provides visual control of the target in the preliminary (coarse) adjustment and focusing of the optical system. The mountable insert makes it possible to obtain a magnified field of vision, which is up to 5 mm (instead of the 1.5-mm field of vision field of the main optical system). A Matrix-440k/12 monochromatic CCD camera (manufactured by DeltaTech, Science Park, M. V. Lomonosov Moscow State University) is used as a photoreceiving element of the insert. A peculiar feature of the camera is that it can operate both in the digital and analog modes (in PAL standard).

A.3. Cryogenic System

Fabrication and study of such a microobject as a cryogenic target is carried out at temperature $T = 20 - 4.2$ K. The requirements on the tomographic experiment – large angular aperture of the optical system, $\sim 60^\circ$, and, therefore, high infiltration heat due to the radiation; limited distance from the object to the objective lens, $\sim$54 mm; resistance of the positioning system to low-frequency vibrations; stability of the object position after cooling to an accuracy of ± 500 μm – necessitated a specialized cryogenic system to be developed, which consists of the cryostat and the cryogenic target-fabrication module. The general view of the cryostat is shown in Fig. 30b.

The cryostat is a modified version of the standard KG-20 model, the lower part of which is equipped with a special tomographic test chamber (TTC). The fabrication module, whose operation is based on the original FST method [2, 15], represents an insert into the cryostat. The operation procedure of the module is described in detail in [12, 21]. The construction of the module provides the fabrication and delivery of a ready unmounted target into the target loading channel (see 1 in Fig. 30d) and further into the positioning device inside the TTC.

Acknowledgments

This work was supported by the International Science and Technology Center under Project No. 1557. The authors are grateful to the Project collaborator Prof. T. Norimatsu (Institute of Laser Engineering,

Osaka University, Japan) and to colleagues at the P. N. Lebedev Physical Institute Dr. A. A. Akunets and Dr. V. M. Dorogotovtsev for providing polystyrene microshells to test the algorithms and components of the diagnostic complex.

References

1. I. V. Aleksandrova, E. R. Koresheva, I. E. Osipov, et al.. *Laser Particle Beams*, **17**, 729 (1999).
2. I. V. Aleksandrova, A. A. Belolipetskiy, V. I. Golov, et al., *Fusion Technol.*, **38**, 190 (2000).
3. T. P. Bernat, D. H. Darling, and J. J. Sanchez, *J. Vac. Sci. Technol.*, **20**, 1362 (1982).
4. V. M. Izgorodin, S. B. Kormer, G. P. Nikolaev, and A. V. Pinegin, *Sov. J. Quantum Electron.*, **16**, 35 (1986).
5. T. R. Pattinson and W. J. Felmlee, *J. Vac. Sci. Technol. A*, **6**, 1882 (1988).
6. M. D. Wittman, D. Malacara, and H.-J. Kong, "High Precision Characterization of Gas-Filled Shells Using Fabry–Perot Interferometer," in: *Laser Interferometry IV: Computer-Aided Interferometry*, *SPIE*, **1553**, 456 (1991).
7. J. A. Koch, T. P. Bernat, G. W. Collins, et al., *Fusion Technol.*, **38**, 123 (2000).
8. H. M. Roder, G. E. Childs, R. D. McCarthy, and P. E. Angerhofer, *Survey of the Properties of the Hydrogen Isotopes below Their Critical Temperatures*, NBS Technical Note (1973), No. 641.
9. E. R. Koresheva, A. I. Nikitenko, I. V. Aleksandrova, et al., *Nucl. Fusion*, **46**, 890 (2006).
10. I. V. Aleksandrova, S.V. Bazdenkov, V. I. Shcherbakov, et al., *J. Appl. Phys. D*, **37**, 1163 (2004).
11. Yu. T. Larin and V. A. Nesterenko, *Polymer Optical Fibers* [http://www.informost.ru/].
12. I. V. Aleksandrova, E. R. Koresheva, I. E. Osipov, et al., *Fusion Technol.*, **38**, 166 (2000).
13. F. Ito, K. Nagai, M. Nakai, et al., *Jpn J. Appl. Phys.*, **45**, L335 (2006).
14. I. S. Grigoryev and U. Z. Meilikhov (eds.), *Physical Magnitudes. A Reference Book* [in Russian], Energoatomizdat, Moscow (1991), p. 46.
15. R. Gloker, *X-Rays and Materials Tests* [in Russian], GTTI, Leningrad (1992), p. 36.
16. *X-Ray Engineering, Reference Manual* [in Russian], Mashinostroenie, Moscow (1980), Vol. 1, p. 14; Vol. 2, p. 179.
17. *General Atomics*, FY01 Annual Report (2002), Report GA-A23852.
18. E. J. Allin and W. F. J. Hare, *Phys. Rev. Lett.*, **98**, 554 (1955).
19. G. W. Collins, D. N. Bittner, and E. Monsler, *J. Vac. Sci. Technol. A*, **14**, 2897 (1996).
20. G. H. Edgell, R. S. Craxton, L. M. Elasky et al., *Fusion Sci. Technol.*, **49**, 616 (2006).
21. I. V. Aleksandrova, E. R. Koresheva, I. E. Osipov, et al., *J. Russ. Laser Res.*, **28**, No. 3 (2007).